

## First Sagittarius A\* Event Horizon Telescope Results. II. EHT and Multi-wavelength Observations, Data Processing, and Calibration

THE EVENT HORIZON TELESCOPE COLLABORATION

### ABSTRACT

We present Event Horizon Telescope (EHT) 1.3 millimeter measurements of the radio source located at the position of the supermassive black hole Sagittarius A\* (Sgr A\*), collected during the 2017 April 5–11 campaign. The observations were carried out with eight facilities at six locations across the globe. Novel calibration methods are employed to account for Sgr A\*'s flux variability. The majority of the 1.3 millimeter emission arises from horizon scales, where intrinsic structural source variability is detected on timescales of minutes to hours. The effects of interstellar scattering on the image and its variability are found to be subdominant to intrinsic source structure. The calibrated visibility amplitudes, particularly the locations of the visibility minima, are broadly consistent with a blurred ring with a diameter of  $\sim 50 \mu\text{as}$ , as determined in later works in this series. Contemporaneous multi-wavelength monitoring of Sgr A\* was performed at 22, 43, and 86 GHz and at near infrared and X-ray wavelengths. Several X-ray flares from Sgr A\* are detected by Chandra, one at low significance jointly with Swift on 2017 April 7 and the other at higher significance jointly with NuSTAR on 2017 April 11. The brighter April 11 flare is not observed simultaneously by the EHT but is followed by a significant increase in millimeter flux variability immediately after the X-ray outburst, indicating a likely connection in the emission physics near the event horizon. We compare Sgr A\*'s broadband flux during the EHT campaign to its historical spectral energy distribution and find both the quiescent and flare emission are consistent with its long-term behaviour.

*Keywords:* black holes – galaxies: individual: Sgr A\* – Galaxy: center – techniques: interferometric

### 1. INTRODUCTION

The first legacy set of papers by the Event Horizon Telescope (EHT) focused on the supermassive black hole M87\* (Event Horizon Telescope Collaboration et al. 2019a,b,c,d,e,f, hereafter M87\* Papers I, II, III, IV, V, and VI), but Sagittarius A\* (Sgr A\*) was the spark that motivated the formation of the EHT. This work presents EHT observations of Sgr A\* at 1.3 mm, which serve as the foundation for the observational and theoretical papers presented in this second legacy series (Event Horizon Telescope Collaboration et al. 2021a,b,c,d,e,f, hereafter Papers I, II, III, IV, V and VI).

Sgr A\* is the black hole at the center of our own Milky Way, and is the only supermassive black hole observable at a distance of a few kiloparsecs. Among all known black holes, Sgr A\* has the largest predicted angular size ( $\sim 50 \mu\text{as}$ , see Paper III and Paper IV, and references therein). It is also a highly variable source, with flickering, flares, and other stochastic processes occurring across the electromagnetic spectrum on short and long timescales. These unique characteristics make Sgr A\* an important laboratory for studying the fundamental physics and astrophysics of black holes at high angular resolution.

Sgr A\* has been observed with millimeter very-long-baseline interferometry (VLBI) for over a quarter cen-

tury. After initial successful 1 mm VLBI tests on quasars (Padin et al. 1990; Greve et al. 1995), Sgr A\* was first successfully detected on a VLBI baseline between the IRAM 30-m telescope on Pico Veleta (PV) in Spain and a single antenna of the Plateau de Bure Interferometer in France in 1995 (Krichbaum et al. 1997). This detection revealed a compact source, with a size of  $(110 \pm 60) \mu\text{as}$  (Krichbaum et al. 1998). Early size measurements at 3 mm and 1 mm were larger than expected (cf. e.g., Lo et al. 1998), indicating that short-wavelength VLBI measures the intrinsic structure in Sgr A\* rather than interstellar scattering along the line of sight. Subsequent VLBI experiments using wider recorded bandwidth and three telescopes with longer baselines provided a tighter estimate of the source size,  $43^{+14}_{-8} \mu\text{as}$ , giving the first unambiguous detection of horizon-scale structure in Sgr A\* (Doeleman et al. 2008). Meanwhile, continued VLBI observations at  $\lambda \gtrsim 3 \text{ mm}$  were better able to characterize the properties of the anisotropic interstellar scattering screen (e.g., Bower et al. 2004a; Johnson et al. 2018a).

Excitement from these VLBI measurements was further galvanized by crucial theoretical and technical advancements made in parallel. Simulations of Sgr A\* by Falcke et al. (2000) demonstrated that a shadow of the sort originally predicted by Bardeen (1973) would be

observable with millimeter-wavelength VLBI.<sup>1</sup> Technological advances greatly increased the capabilities of the growing EHT, as detailed in M87\* Paper II. These advances led to a new era in which the detection of Sgr A\* on long baselines at 1 mm became routine (Fish et al. 2011; Johnson et al. 2015; Fish et al. 2016; Lu et al. 2018). Most significantly, the phased Atacama Large Millimeter/submillimeter Array (ALMA) (Matthews et al. 2018) participated in its first EHT science observations in 2017, along with other antennas that added to the baseline coverage. Indeed, data from these observations produced the M87\* total-intensity (M87\* Paper I; M87\* Paper II; M87\* Paper III; M87\* Paper IV; M87\* Paper V; M87\* Paper VI) and polarization results (Event Horizon Telescope Collaboration et al. 2021g,h, Papers VII and VIII hereafter), as well as high angular resolution images of extragalactic radio jets (Kim et al. 2020; Janssen et al. 2021). These data also motivate the Sgr A\* results in this series.

As these VLBI discoveries were advancing, Sgr A\* was also being studied intensively at other wavelengths. Radio, millimeter, infrared, and X-ray observations showed that Sgr A\* has both a very low bolometric-to-Eddington luminosity ratio of  $L/L_{\text{Edd}} \sim 10^{-9}$  (Genzel et al. 2010), and a very low mass accretion rate of  $\sim 10^{-9}$  to  $10^{-7} M_{\odot} \text{ yr}^{-1}$  (Baganoff et al. 2003a; Marrone et al. 2006a, 2007; Shcherbakov et al. 2012; Yusef-Zadeh et al. 2015). At most wavelengths, Sgr A\*'s flux can be decomposed into a quiescent and variable component.

In the X-ray, Sgr A\* is a persistent source, with a flux of about  $3 \times 10^{33} \text{ erg s}^{-1}$  (Baganoff et al. 2001, 2003a) from thermal bremsstrahlung radiation originating from hot plasma near the Bondi radius (e.g., Quataert 2002; Baganoff et al. 2003a; Yuan et al. 2003; Liu et al. 2004; Wang et al. 2013). Bright X-ray flares punctuate this emission about once per day and are characterized by non-thermal emission centered on the black hole (e.g., Neilsen et al. 2013a). Near infrared (NIR) detections of Sgr A\* also reveal a highly variable source, with emission peaks observed more frequently than in the X-ray (Genzel et al. 2003; Ghez et al. 2004; Gravity Collaboration et al. 2020). Both the X-ray and NIR variability occur on timescales of several hours, consistent with emission originating near the black hole's innermost stable circular orbit (ISCO), which depends on the black hole's mass and spin. Sgr A\*'s mid-IR flux is only marginally detected (e.g., Iwata et al. 2020) or it can be inferred indirectly from model fitting.

Millimeter polarimetry of Sgr A\* reveals linearly polarized flux from an emitting region of  $\sim 10$  Schwarzschild radii ( $R_S$ ), which indicates a dense magnetized accretion flow again extending out to the Bondi

radius. Bower et al. (2018) find a mean rotation measure (RM) of  $\sim -5 \times 10^5 \text{ rad m}^{-2}$  that can be modeled as a radiatively inefficient accretion flow (RIAF) with an accretion rate of  $\sim 10^{-8} M_{\odot} \text{ yr}^{-1}$ . Circular polarization is also detected at a mean value of  $-1.1 \pm 0.2\%$ . Both the RM and the circular polarization are variable on timescales of hours to months (Bower et al. 2018).

Similarly, observations of Sgr A\* between 15 and 43 GHz reveal variability at the 5–10% level on timescales shorter than four days (Macquart & Bower 2006). Sgr A\*'s flux density distribution at 217.5, 219.5, and 234.0 GHz was investigated recently by Iwata et al. (2020); they find variability on timescales of  $\sim$  tens of minutes to hours, indicating that the emission at these wavelengths is also likely to arise near the ISCO.

Hence, in addition to the excitement around resolving Sgr A\*'s intrinsic structure at 1.3 mm, it became clear that multi-wavelength observations during the EHT campaign would offer the first opportunity to definitively connect the black hole's variable flux components with changes observed at horizon scales.

In this work we present the first EHT 1.3 mm observations of Sgr A\*, alongside multi-wavelength data collected contemporaneously in April 2017. Contemporaneous interferometric array data from ALMA and SMA have been analyzed and are described here (and presented in more detail in a companion paper, Wielgus et al. 2022). The campaign also includes observations from the East Asian VLBI Network (EAVN), the Global 3 mm VLBI Array (GMVA), the Very Large Telescope (VLT), the Neil Gehrels Swift Observatory, the Chandra X-ray Observatory, and the Nuclear Spectroscopic Telescope (NuSTAR). These coordinated observations provide (quasi-)simultaneous multi-wavelength coverage with exceptional spatial and spectral resolution. Since variability at timescales of minutes to hours can be probed on horizon scales by the EHT, and on a range of other spatial (and spectral) scales by these other observatories, combining them into a single “snapshot” spectral energy distribution (SED) maximizes the broadband constraints that the observations can place on theoretical models.

This manuscript (Paper II) is organized as follows. In Section 2 we present an overview of the 2017 EHT observing campaign. Section 3 delves more deeply into the EHT data calibration and reduction specific to these Sgr A\* data. Section 4 outlines the multi-wavelength (MWL) campaigns that accompanied the EHT observations. Section 5 describes the resulting EHT and MWL data products, including those provided via a public data archive, and discusses these new observations in the context of longer-term monitoring campaigns that have characterized Sgr A\*'s variability over more than 20 years. We offer a brief summary and conclusions in Section 6.

<sup>1</sup> More details about the appearance of black holes are given in M87\* Paper I.

## 2. EVENT HORIZON TELESCOPE OBSERVING CAMPAIGN

The first EHT observations of Sgr A\* were collected in April 2017, alongside contemporaneous broadband data — the coverage is shown in Figures 1 and 2. A detailed description of the EHT array and its instrumentation can be found in M87\* Paper II, with further details related to the 2017 observing campaign in M87\* Paper III. Here we provide a brief summary of this material, along with details pertinent to the observations of Sgr A\* and associated calibration sources.

EHT observations were carried out with eight observatories at six locations: ALMA and the Atacama Pathfinder Experiment (APEX) on the Llano de Chajnantor in Chile, the Large Millimeter Telescope Alfonso Serrano (LMT) on Volcán Sierra Negra in Mexico, the James Clerk Maxwell Telescope (JCMT) and Submillimeter Array (SMA) on Maunakea in Hawai‘i, IRAM 30m Telescope on Pico Veleta (PV) on Pico Veleta in Spain, the Submillimeter Telescope (SMT) on Mt. Graham in Arizona, and the South Pole Telescope (SPT) in Antarctica. The locations of these telescopes are plotted in Figure 1 of Paper I.

Sgr A\* was observed on five nights: 2017 April 5, 6, 7, 10, and 11. ALMA did not participate in the array for observations of Sgr A\* on 2017 April 5 or 10. PV observed Sgr A\* only on 2017 April 7. Weather conditions were good or excellent at all sites on all five observing nights. Median opacities on each night are provided in M87\* Paper III. In this series of papers, we focus our analysis on April 6 and 7, which have the best  $(u, v)$ -coverage.

Two bands of approximately 2 GHz each were observed, centered at sky frequencies of 227.1 and 229.1 GHz (“low” and “high” bands, respectively). Single-dish stations recorded a 2-bit Nyquist-sampled bandwidth of 2048 MHz per polarization using Reconfigurable Open Architecture Computing Hardware 2 (ROACH2) digital backends (Vertatschitsch et al. 2015). The SMA observed using six or seven telescopes (depending on the observing night) whose signals were summed using the SMA Wideband Astronomical ROACH2 Machine (SWARM; Primiani et al. 2016; Young et al. 2016). Since SWARM produces data in the frequency domain at a different sampling rate than at other observatories, SMA data require a post-observation, pre-correlation pass through the Adaptive Phased-array and Heterogeneous Interpolating Down-sampler for SWARM (APHIDS; see also the Appendix of M87\* Paper II). ALMA observed as a phased array of 35–37 telescopes using the ALMA Phasing System (Matthews et al. 2018). Data were recorded onto Mark 6 VLBI Data Systems (Whitney et al. 2013).

All but two observatories recorded both left and right circular polarization (LCP and RCP respectively). The JCMT was equipped with a single-polarization receiver

that observed RCP on 2017 April 5–7 and LCP on 2017 April 10–11. ALMA recorded both linear polarizations (X and Y).

The schedule consisted of scans of Sgr A\* interleaved with scans of NRAO 530 (J1733–1304) and J1924–2914 as calibration sources. On 2017 April 6, observations commenced after the preceding target source, M87, set at ALMA. Generally, two eight-minute scans of Sgr A\* were followed by a short (typically, three-minute) scan on a calibrator, with an eight-minute gap approximately every hour. The 2017 April 7 schedule, which did not include M87, started when Sgr A\* rose above the 20° elevation limit at ALMA. Scan lengths on Sgr A\* for this schedule were dithered between five and twelve minutes to reduce the effects of periodic sampling on detection of time variability associated with the ISCO period. On both nights, Sgr A\* was observed until the source set below the local horizon at the SMT and LMT, which happens at approximately the same time. The scan coverage for these nights is shown in Figure 1.

Data were correlated with the Distributed FX (DiFX) software correlation package (Deller et al. 2011) at the two correlator centers at the Max-Planck-Institut für Radioastronomie in Bonn, Germany and MIT Haystack Observatory in Westford, Massachusetts; for details see M87\* Paper III. The CALC model was used for an a priori correction of rates and delays. Multiple correlation passes were required to diagnose and mitigate data issues, as discussed in the Appendix of M87\* Paper III; parameters hereafter refer to those for the final correlation (Rev7) used for science-release data. The final correlation produced 32 baseband channels, each 58 MHz wide with a spectral resolution of 0.5 MHz, and averaged to a 0.4 s accumulation period. The Sgr A\* correlation center was set to  $\alpha_{J2000} = 17^{\text{h}}45^{\text{m}}40^{\text{s}}.0356$ ,  $\delta_{J2000} = -29^{\circ}00'28''.240^2$ , based on the position of Reid & Brunthaler (2004) corrected to the epoch of observation for the apparent motion introduced by the orbit of the solar system around the Galaxy. The corrected position produced smaller residual delays and rates compared with the uncorrected position, resulting in a minor improvement in sensitivity. Subsequent to correlation, PolConvert (Martí-Vidal et al. 2016) was run to convert the mixed-polarization data products (XL, XR, YL, YR) to the circular basis on ALMA baselines, as described in Goddi et al. (2019).

## 3. EHT DATA CALIBRATION AND REDUCTION

In this section, we summarize the EHT data calibration pathway and highlight aspects that are particular for the Sgr A\* data. A comprehensive description of the EHT data reduction methods, combined with a re-

<sup>2</sup> This position for Sgr A\* is also adopted in the multi-wavelength analysis that follows.

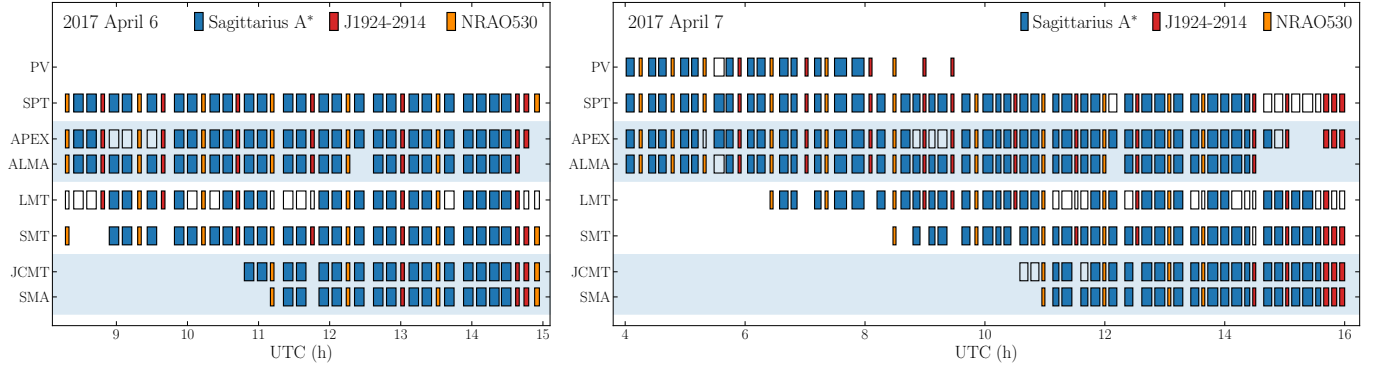


**Figure 1.** EHT 2017 observing schedules for Sgr A\* and its calibrators (J1924–2914 and NRAO530), covering observations on April 6–7 2017. Empty rectangles represent scans that were scheduled but not observed successfully due to weather or technical issues. The filled rectangles represent scans corresponding to detections available in the final data set. Scan durations vary between 3 and 12 minutes, as reflected by the width of each rectangle. ALMA/APEX and JCMT/SMA are pairs of co-located stations (enclosed in light blue shaded regions), providing the same  $(u, v)$ -coverage.

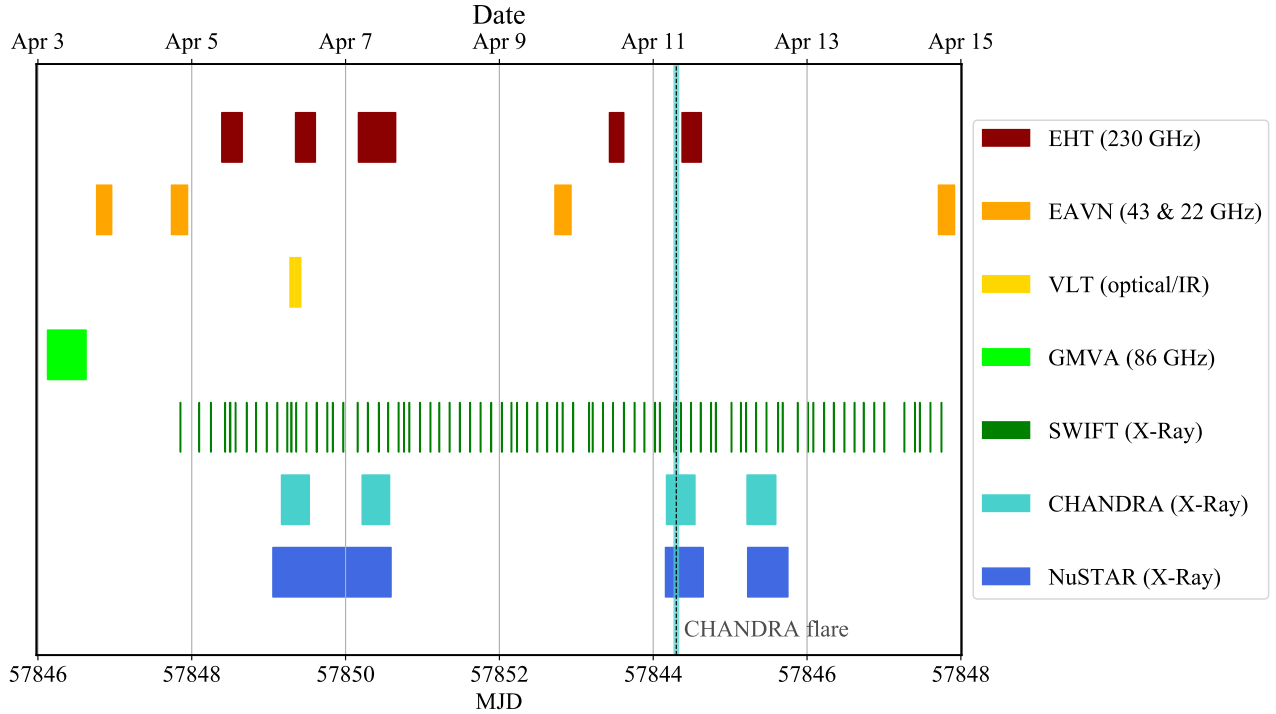


**Figure 2.** Instrument coverage of Sgr A\* during the 2017 April 3–15 multi-wavelength observing campaign, which includes the East Asian VLBI Network (EAVN), the Global 3mm VLBI Array (GMVA), the Very Large Telescope (VLT), the Neil Gehrels Swift Observatory (SWIFT), the Chandra X-ray Observatory (CHANDRA), and the Nuclear Spectroscopic Telescope (NuSTAR). For the EHT data described in this work we focus on April 6 and 7, which have the best  $(u, v)$ -coverage and for which detailed instrument and source coverage is shown in Figure 1. Details of the multi-wavelength campaign and spectral energy distribution are contained in Sections 4 and 5.2.1.



cap of VLBI data calibration fundamentals, is given in M87\* Paper III.

### 3.1. Processing pipelines

To reduce the volume of the data and to accumulate signal-to-noise ratio ( $S/N$ ), we average the visibilities in time and frequency. To avoid non-closing errors, we must stabilize the signal by removing all significant external data corruption effects that have not been captured by the correlator model beforehand. We apply scaling corrections as a function of time to the visibilities to ensure unity auto-correlations. Additionally, phase errors induced by atmospheric turbulence on second time scales must be modeled and removed (M87\* Paper III). Along the frequency axis, residual post-CALC delays—phase slopes over the frequency band—are caused primarily by atmospheric path-length variations. No significant instrumental delay effects are present in our digital recording system. However, imperfect amplitude- and phase-bandpass responses impact the data and must be corrected.

We have developed two independent VLBI data reduction pipelines to perform these pre-averaging calibration steps to stabilize the signal: EHT-HOPS (Blackburn et al. 2019), which is based on the Haystack Observatory Postprocessing System (HOPS) (Whitney et al. 2004) software and rPICARD (Janssen et al. 2018, 2019b), which is based on the Common Astronomy Software Applications (CASA) (McMullin et al. 2007; van Bemmelen et al. 2019) package. The other papers in this series make use of the data produced from both pipelines, whose consistency has been established in M87\* Paper III, for a verification of scientific results. The AIPS-based (Greisen 2003) pipeline that has also been used for the M87\* EHT results (M87\* Paper III) is no longer being maintained.

EHT-HOPS processes data that have been converted into Mark4 format by DiFX task `difx2mark4`. These correlation coefficients have been normalized to unity autocorrelation at  $0.4\text{ s} \times 58\text{ MHz}$  resolution and then scaled to idealized analog correlation amplitudes according to the 2-bit quantization efficiency correction factor  $\sim 1/0.88$ . Baseline rate and delay solutions are fit with the HOPS `fourfit` routine. These fringe solutions are then “globalized” into station-based corrections using a least-squares method (similar to Alef & Porcas 1986). A stable phase bandpass response for each antenna is derived using an ensemble of high  $S/N$  detections on bright calibrators and applied to all data. Turbulent phases introduced by the troposphere are corrected by fitting a piecewise polynomial phase model to the visibilities from baselines connected to the most sensitive station in each scan. To avoid overfitting to thermal noise, the phases of each 58 MHz spectral window are independently corrected using a model derived from the other, remaining 31 spectral windows. Finally, the geometric feed rotation angle evolution is corrected and rel-

ative complex gains between the RCP and LCP signal paths are fitted. We commonly refer to the calibrated data produced by the EHT-HOPS pipeline as “HOPS” data.

rPICARD follows the Hamaker-Bregman-Sault measurement equation (Hamaker et al. 1996; Smirnov 2011a,b,c,d) as implemented in the CASA framework. For the amplitude calibration, the CASA `accor` task is used to enforce unity auto-correlations, correcting for digital sampler biases. As this task scales the visibilities at the 58 MHz resolution, it also corrects for the gross amplitude bandpass of each station. Residual amplitude-bandpass effects are removed with a custom bandpass calibration table formed by taking the median of the normalized 0.5 MHz channelized auto-correlations of all VLBI scans combined. The phases are corrected with the `fringe` task, which performs a global Schwab & Cotton (1983) fringe-fit assuming an unpolarized point source model. The data are segmented into the shortest bins within the expected atmospheric coherence time, where a sufficiently high  $S/N$  can be accumulated to obtain fringe detections. These detections are then used to correct for atmospheric phase turbulence and small residual delay variations that can occur within VLBI scans. A crude phase bandpass at 58 MHz is solved with a “single-band fringe-fit”, where we apply the solutions from the scan with the highest  $S/N$  fringe solution per antenna. The residual 0.5 MHz phase bandpass is corrected with the CASA `bandpass` task with a  $S/N > 3$  cutoff using the data of all calibrator scans combined. Geometric feed rotation angles are corrected for on-the-fly, following the measurement equation, and no relative complex gains are corrected in the CASA data. We commonly refer to the calibrated data produced by the rPICARD pipeline as “CASA” data.

The EHT VLBI data indicate a phase offset (either constant, or with a time-dependent drift component) between the two polarization channels that can be attributed largely to instrumental effects, and in a small part to circular polarization (Stokes  $\mathcal{V}$ ) of the source. The instrumental phase shifts are corrected through polarimetric gain ratio calibration, aligning RR and LL components to compute the total-intensity (Stokes  $\mathcal{I}$ ) visibilities coherently. Leveraging the facts that the RCP–LCP instrumental phase of ALMA after PolConvert is zero (Martí-Vidal et al. 2016; Goddi et al. 2019) and that intrinsic Stokes  $\mathcal{V}$  signals will have a negligible phase contributions on ALMA baselines, the parallel hand signals have been aligned for each VLBI scan under the assumption of  $\mathcal{V} = 0$  on ALMA baselines. The same strategy is also employed inherently by rPICARD, as the parallel correlation products are fringe-fitted separately. As the phase calibration is station-based, intrinsic Stokes  $\mathcal{V}$  signals are not removed from the data. More details about the EHT data reduction pipelines,

**Table 1.** Fitted LMT gains on each EHT observing day.

UTC Day (April 2017)	RCP DPFU (Jy/K)	LCP DPFU (Jy/K)
05	$0.046 \pm 0.003$	$0.048 \pm 0.003$
06	$0.032 \pm 0.009$	$0.034 \pm 0.009$
07	$0.061 \pm 0.001$	$0.064 \pm 0.001$
10	$0.076 \pm 0.001$	$0.077 \pm 0.001$
11	$0.067 \pm 0.005$	$0.067 \pm 0.004$

including flow-charts of their processing steps, and detailed verification tests are given in M87\* Paper III.<sup>3</sup>

Due to the excellent sensitivity of the EHT, we have a high  $S/N$  on many baselines probing Sgr A\*, which allows us to model atmospheric phase fluctuations occurring on short timescales to effectively extend the coherence time (M87\* Paper III). Combined with the small field of view around the VLBI correlation phase center of the EHT, this means that reasonable averaging intervals are limited primarily by the spectral and temporal variations of the target. With a fractional bandwidth of  $\sim 1\%$ , we can safely average the data over our observing bandpass without introducing considerable bandwidth smearing effects (Thompson et al. 2017). On the other hand, Sgr A\* is known to vary on very short timescales, possibly down to the gravitational timescale of  $\sim 21$  s. We have therefore chosen to average our data, which was correlated with a 0.4 s period, into 10 s time bins.

### 3.2. Flux density scaling

To scale our correlation coefficient measurements to a physical flux density unit scale, we estimate the system equivalent flux density (SEFD) of every station in the array. The SEFD of a single antenna or phased-up array is given as

$$\text{SEFD} = \frac{T_{\text{sys}}^*}{\eta_{\text{ph}} \text{gc}(E) \text{DPFU}}. \quad (1)$$

Here,  $T_{\text{sys}}^*$  is the effective system temperature, which characterizes the total noise contribution along a station’s signal path and corrects for the signal attenuation caused by the Earth’s atmosphere. The phasing efficiency of a phased array is given by  $\eta_{\text{ph}}$ , which is unity for single dish stations. The station gain is factored into a normalized elevation ( $E$ ) gain curve  $\text{gc}(E)$  and the “degrees-per-flux-unit” (DPFU) conversion factor between measured system temperatures and

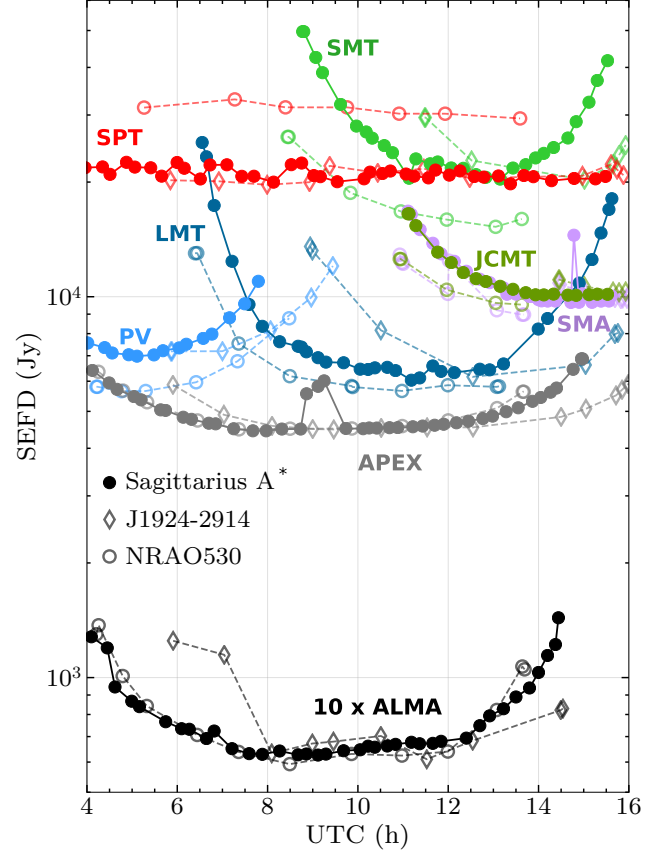


**Figure 3.** Example of system equivalent flux density (SEFD) values during a single night of the 2017 EHT observations (2017 April 7, high-band RCP). Values for Sgr A\* are marked with full circles, values for J1924–2914 are marked with empty diamonds, and values for NRAO 530 are marked with empty circles. ALMA SEFDs have been multiplied by 10 in this plot for visualization purposes.

flux densities. The DPFU is determined by the aperture efficiency  $\eta_{\text{ap}}$  and total collecting area  $A_{\text{geom}}$  as  $\text{DPFU} = \eta_{\text{ap}} A_{\text{geom}} / (2k_{\text{B}})$ , with  $k_{\text{B}}$  the Boltzmann constant. We can scale a correlation coefficient  $r_{i-j}$  measured on a baseline  $i-j$  in units of thermal noise, to a visibility  $V_{i-j}$  in units of Jy via

$$V_{i-j} = \sqrt{\text{SEFD}_i \text{SEFD}_j r_{i-j}}. \quad (2)$$

We have performed this flux density calibration with a common framework<sup>4</sup> for both the CASA and HOPS data. Compared to the SEFDs used to calibrate the data released for M87\* and 3C 279 (M87\* Paper III), we have updated several a priori calibration parameters. We are using the Butler (2012) planet models (updated for the year 2017) for the gain calibration of the APEX, PV, and SMT telescopes, instead of the previously used

<sup>3</sup> Note that the M87\* HOPS data presented in M87\* Paper III were obtained with multi-source, multi-day calibration of the polarimetric gain ratios (Steel et al. 2019). While the aim of this method was to preserve the Stokes  $V$  structure of the resolved images, it indicated underfitting of the instrumental effects, potentially increasing the resulting systematic errors.

<sup>4</sup> <https://github.com/sao-eh/eat>

GILDAS<sup>5</sup> models. Additionally, we have used 10.1'' instead of 8.5'' as an updated estimate for the beam size of the LMT and subsequently fitted for the variable station gain on a per-day basis (Table 1).

Data from SMA were re-analyzed, using the intra-SMA interferometric data to derive new SEFD estimates for the phased array data. Aperture efficiencies were calculated using observations of the solar system objects Callisto, Ganymede, and Titan, using the brightness temperature models from Butler (2012), and derived separately for low and high band. Amplitude gain solutions were derived using two quasars—NRAO 530 and J1924–2914—that were observed periodically during the observations of Sgr A\*. Phase-only self-calibration was applied to the SMA interferometer data of Sgr A\*, assuming a point-source model and excluding baselines shorter than 15 kλ in length, due to the presence of large-scale emission features. The resultant gain solutions were used to re-derive phasing efficiencies for the beamformed data used for VLBI analysis. More details about the SMA data reduction are given in Wielgus et al. (2022) Section 2.3.

Typical SEFDs used to calibrate the Sgr A\* flux density are shown in Figure 3. For the time-averaged spectral energy distribution (SED) data gathered in Table 2, we calculate a flux density of  $2.4 \pm 0.2$  Jy between 213 – 229 GHz.

### 3.2.1. Light curves of Sgr A\* and ALMA-VLBI amplitude calibration

The ALMA Phasing System is designed to construct a summed, formatted VLBI signal without interrupting the data stream of each individual antenna, thus allowing the ALMA correlator to compute all of the intra-ALMA visibilities at the same time (Matthews et al. 2018). The calibration information related to these intra-ALMA visibilities is needed for the correct polarimetric processing of the ALMA-VLBI signal (Martí-Vidal et al. 2016; Goddi et al. 2019, 2021).

At the spatial scales sampled by the intra-ALMA baselines, the Sgr A\* field consists of the sum of two components: a point-like source located at the field center and with a time-dependent flux density (i.e., the AGN), and an extended structure that covers several arcseconds, with a total flux of about 1.1 Jy and a surface brightness of about 0.12 Jy/beam (Wielgus et al. 2022). This extended component is known as the “minispiral”, and its emission is related to ionized gas and dust in the galactic center (e.g., Lo & Claussen 1983).

The use of the intra-ALMA self-calibration gains to compute the corrections for the VLBI amplitudes of the ALMA-related baselines provides a very accurate determination of the relative changes in the ALMA’s VLBI amplitude gains (Goddi et al. 2019). However, this ap-

proach has important limitations for the correct calibration of a time-variable source like Sgr A\* (Figure 4). In particular, the use of an a priori (constant) model for the amplitude self-calibration of the Sgr A\* intra-ALMA visibilities results in an incorrect estimate of the phased-ALMA amplitude scaling. To overcome this limitation, we calibrate the Sgr A\* ALMA gains with the source’s light curve, which is computed under the assumption that the flux density distribution of the minispiral remains stable across the extent of the observations (Wielgus et al. 2022).

We note that, even though the minispiral modeling allows us to calibrate relative ALMA gains at the  $\sim 1\%$  level, a constant  $\sim 10\%$  calibration uncertainty remains for the overall gain of the phased array, which is tied to the estimated flux density of Ganymede (the source used as primary calibrator, Goddi et al. 2019).

We perform a time-dependent variant of network calibration (M87\* Paper III) of the EHT VLBI data to a merged light curve from ALMA and the SMA (Figure 4). The ALMA light curve is computed through the minispiral method described above and a description of the SMA light curve is given in Wielgus et al. (2022). The two light curves are combined by leveling the median amplitudes in the overlapping time between ALMA and SMA and a smoothing spline interpolation in time. The network calibration procedure leverages the presence of co-located sites, constraining gains of telescopes with a co-located partner by assuming that intra-site baselines (ALMA–APEX and JCMT–SMA; see Figure 1) observe a point source with a time-dependent flux density, corresponding to the light curve.

## 4. MULTI-WAVELENGTH OBSERVING CAMPAIGN

In addition to the ALMA and SMA millimeter light curves collected as a part of the EHT observations (Wielgus et al. 2022), the 2017 Sgr A\* EHT campaign includes observations from elite ground-based facilities (§4.1), including the East Asian VLBI Network, the Global 3 mm VLBI Array, the Very Large Telescope, as well as space-based telescopes (§4.2) including the Neil Gehrels Swift Observatory, the Chandra X-ray Observatory, and the Nuclear Spectroscopic Telescope. Figure 2 shows coverage of Sgr A\* for each of these instruments during the campaign. These coordinated observations provide (quasi-)simultaneous wavelength coverage and enable detailed multi-wavelength variability studies that place broadband constraints on models (see Paper V and Paper VI). We describe these observations briefly here and place them in the broader EHT and Sgr A\* historical context in Section 5.2.

### 4.1. Supplementary Ground-based Observations

#### 4.1.1. East Asian VLBI Network

The East Asian VLBI Network (EAVN; e.g., Wajima et al. 2016; An et al. 2018; Cui et al. 2021) consists of

<sup>5</sup> <http://www.iram.fr/IRAMFR/GILDAS>

**Table 2.** Values for the Sgr A\* SED observed by coordinated ground-based and space-based observatories during the EHT 2017 run.

Observatory	Frequency [GHz]	$\nu F_\nu$ [ $\times 10^{-12} \text{ erg s}^{-1} \text{ cm}^{-2}$ ]	Flux [Jy]	$\nu L_\nu$ [ $\times 10^{34} \text{ erg s}^{-1}$ ]
EAVN	22	$0.24 \pm 0.02$	$1.07 \pm 0.11$	$0.19 \pm 0.02$
EAVN	43	$0.58 \pm 0.06$	$1.35 \pm 0.14$	$0.48 \pm 0.05$
GMVA	86	$1.63 \pm 0.17$	$1.9 \pm 0.2$	$1.3 \pm 0.1$
GMVA	88	$1.67 \pm 0.18$	$1.9 \pm 0.2$	$1.4 \pm 0.1$
GMVA	98	$1.96 \pm 0.20$	$2.0 \pm 0.2$	$1.6 \pm 0.2$
GMVA	100	$2.10 \pm 0.20$	$2.1 \pm 0.2$	$1.67 \pm 0.2$
ALMA/SMA <sup>a</sup>	213-229	$5.28 \pm 0.44$	$2.4 \pm 0.2$	$4.3 \pm 0.4$
VLT	$1.38 \times 10^5$	$< 4.12$	$< 0.003$	$< 3.4$
Chandra/NuSTAR	$5.68 \times 10^8$	$0.70^{+0.15}_{-0.20}$	$1.23^{+0.27}_{-0.35} \times 10^{-7}$	$0.57^{+0.13}_{-0.16}$
Chandra/NuSTAR	$7.84 \times 10^8$	$0.49^{+0.06}_{-0.11}$	$6.27^{+0.74}_{-1.40} \times 10^{-8}$	$0.40^{+0.05}_{-0.09}$
Chandra/NuSTAR	$1.08 \times 10^9$	$0.33^{+0.01}_{-0.05}$	$3.09^{+0.11}_{-0.46} \times 10^{-8}$	$0.27^{+0.01}_{-0.04}$
Chandra/NuSTAR	$1.49 \times 10^9$	$0.25^{+0.25}_{-0.04}$	$1.71^{+1.71}_{-0.25} \times 10^{-8}$	$0.21^{+0.21}_{-0.03}$
Chandra/NuSTAR	$2.06 \times 10^9$	$0.08^{+0.09}_{-0.02}$	$0.39^{+0.43}_{-0.11} \times 10^{-8}$	$0.06^{+0.07}_{-0.02}$
Chandra <sup>b</sup>	$1.57 \times 10^9$	$5.63^{+5.06}_{-3.36}$	$3.6^{+3.2}_{-2.1} \times 10^{-7}$	$4.61^{+4.15}_{-2.76}$
NuSTAR <sup>b</sup>	$9.55 \times 10^9$	$0.78^{+0.86}_{-0.73}$	$8.3^{+9.0}_{-7.6} \times 10^{-9}$	$0.64^{+0.70}_{-0.60}$

<sup>a</sup>Mean measurement across 213-229 GHz. The spectral index at these frequencies was observed to be close to zero (Wielgus et al. 2022)

<sup>b</sup>2017 April 11 X-ray flare.

NOTE—Frequencies for X-ray observatories reflect the central frequency of the keV energy band within the observation bin.

the 7 telescopes of KaVA (KVN<sup>6</sup> and VERA<sup>7</sup> Array; e.g., Lee et al. 2014; Niinuma et al. 2015), and additional telescopes of the Japanese VLBI Network (JVN; e.g., Doi et al. 2006) and the Chinese VLBI Network (CVN; e.g., Zheng 2015). During the EHT 2017 window, four EAVN observations were carried out at 22 and 43 GHz (Figure 2). A single, symmetric Gaussian model was found to describe the intrinsic structure of Sgr A\* at both wavelengths. The measured flux densities from Sgr A\* at these frequencies are  $(1.07 \pm 0.11)$  Jy and  $(1.35 \pm 0.14)$  Jy, respectively (Table 2). Two of the on 2017 April 3 and 4 are (quasi-)simultaneous with the Global 3 mm VLBI Array observations (Section 4.1.2) as well as the EHT sessions (Cho et al. 2022). These measurements provide an estimated size and flux density of Sgr A\* at 1.3 mm via extrapolation of power-law models (i.e., the intrinsic size scales with observing wavelength as a power-law with an index of  $\sim 1.2 \pm 0.2$ ).

#### 4.1.2. Global 3 mm VLBI Array

VLBI observations of Sgr A\* at 86 GHz were conducted on 2017 April 3 with the Global Millimeter VLBI

Array (GMVA)<sup>8</sup>. Eight Very Long Baseline Array antennas equipped with 86 GHz receivers, the Robert C. Byrd Green Bank Telescope (GBT), the Yebes 40 m telescope, the Effelsberg 100 m telescope, PV, and 37 phased ALMA antennas participated in the observation (project code MB007, published in Issaoun et al. 2019b).

The data were recorded with a bandwidth of 256 MHz for each polarization and fringes were detected out to 2.3 Gλ. The total on-source integration time on Sgr A\* was 5.76 hr over a 12 hr track, with ALMA co-observing for 8 hr. The results of the experiment rule out jet-dominated radio emission models of Sgr A\* with large viewing angles ( $> 20$  deg) and provide stringent constraints on the amount of refractive noise added by the interstellar scattering screen towards the source (Issaoun et al. 2019b), discussed in more detail in Section 5.1.4. The total flux density measured at 86 GHz is  $(1.9 \pm 0.2)$  Jy (Table 2).

#### 4.1.3. Very Large Telescope

The Paranal Observatory’s Nasmyth Adaptive Optics System (NAOS) and Near-Infrared Imager and Spectrograph (CONICA) instrument on the Very Large Telescope (VLT), also known as VLT/NACO, measured a K-band near infrared upper limit of 3 mJy during the 2017 April 7 EHT observing run (courtesy of the MPE Galac-

<sup>6</sup> Korean VLBI Network: three 21 m telescopes in Korea (Yonsei, Ulsan, and Tamna)

<sup>7</sup> VLBI Exploration of Radio Astrometry: four 20 m telescopes in Japan (Mizusawa, Iriki, Ogasawara, and Ishigakijima)

<sup>8</sup> <https://www3.mpifr-bonn.mpg.de/div/vlbi/globalmm/>



tic Center Team). Ongoing observations with the new Very Large Telescope Interferometer GRAVITY instrument (VLTI/GRAVITY, Gravity Collaboration et al. 2017) indicate that Sgr A\*’s typical flux distribution in the NIR K-band changes slope at a median flux density of  $1.1 \pm 0.3$  mJy, characteristic of Sgr A\*’s quiescent NIR emission (Gravity Collaboration et al. 2020).

## 4.2. Coordinated Space-based Observations

### 4.2.1. Neil Gehrels Swift Observatory

Observations from the Swift X-ray Telescope (XRT, Gehrels et al. 2004; Burrows et al. 2005) were reprocessed with the latest calibration database files and the Swift tools contained in HEASOFT-v6.20<sup>9</sup>. Source flux in the 2–10 keV energy band is extracted from a  $10''$  radius circular region centred on the position of Sgr A\*. Count rates are reported as measured (e.g., Degenaar et al. 2013a), i.e., without any correction for the known significant absorption along the Sgr A\* sightline ( $N_H \sim 9 \times 10^{22} \text{ cm}^{-2}$ ).

There are 48 Swift observations of the Galactic center between 2017 April 5 and 2017 April 12, with a total exposure time of 26.3 ks (Figure 2). These observations include a dedicated dense sampling schedule to coincide with the EHT observing window and two observations from the regular Galactic center monitoring program (Degenaar et al. 2013b, 2015; van den Eijnden et al. 2021). The average exposure time of the dense sampling was  $\sim 500$  s, with an average interval between observations of  $\sim 3.5$  hr.

In the 2017 April 7 Swift observation that overlaps the EHT window (Figure 4), a 2–10 keV flux is detected ( $0.023 \text{ ct s}^{-1}$ ) in excess of the 2017  $2\sigma$  trend-line ( $0.018 \text{ ct s}^{-1}$ ), as measured from the cumulative flux distribution observed from Sgr A\*. None of the Swift observations are simultaneous with the 2017 April 11 Chandra flare described in the following section.

### 4.2.2. Chandra X-ray Observatory

A series of Chandra X-ray Observatory (Weisskopf et al. 2002) exposures of Sgr A\* were acquired on 2017 April 6, 7, 11, and 12 using the ACIS-S3 chip in FAINT mode with a  $1/8$  subarray (observations IDs 19726, 19727, 20041, 20040; PI: Garmire), for a total of  $\sim 133$  ks coordinated with the EHT campaign (Figure 2). The small subarray mitigates photon pileup during bright Sgr A\* flares, as well as contamination from the magnetar SGR J1745–2900, which peaked at X-ray wavelengths in 2013 and has faded over the more than 6 years since (Mori et al. 2013; Rea et al. 2013, 2020; Coti Zelati et al. 2015, 2017). It also achieves a frame rate of 0.44 s vs. Chandra’s standard rate of 3.2 s.

Chandra data reduction and analysis are performed with the CIAO v4.13 package<sup>10</sup> (Fruscione et al. 2006), CALDB v4.9.4. We use the `chandra_repro` script to reprocess the level 2 events files, update the WCS coordinate system (`wcs_update`), and apply barycentric corrections to the event times (`axbary`). The 2–8 keV light curves are then extracted from a circular region of radius  $1.25''$  centered on the radio position of Sgr A\*. Light curves for 2017 April 6, 7 and 11 are shown in Figure 4. Using the Bayesian Blocks algorithm (Scargle 1998; Scargle et al. 2013; Williams et al. 2017), we search these light curves for flares and robustly detect one on 2017 April 11, with a second weaker detection on April 7 (orange histograms overplotted on the Chandra light curves in Fig. 4).

We use `specextract` to extract X-ray spectra and response files from a similar  $1.25''$  region, centered on Sgr A\*. Since our primary interest for this dataset is the flare emission, we do not extract background spectra from a separate spatial region. Instead, spectra of the quiescent off-flare intervals play the role of our background spectra.

The flare and off-flare intervals are identified by analyzing the X-ray light curves of each observation. For the easily detectable flare on 2017 April 11 (observation ID 20041), we use the direct Gaussian fitting method presented in Neilsen et al. (2013a). For 2017 April 7 (observation ID 19727), we use the Bayesian Blocks decomposition (Scargle 1998; Scargle et al. 2013; Williams et al. 2017); this method is better suited to detecting the sustained low-level activity apparent toward the end of the observation.

### 4.2.3. Nuclear Spectroscopic Telescope Array

X-ray observations from the Nuclear Spectroscopic Telescope Array (NuSTAR Harrison et al. 2013) performed three Sgr A\* observations from 2017 April 6 to 2017 April 11 (observation IDs: 30302006002, 30302006004, 30302006006). These provide a total exposure time of  $\sim 103.9$  ks and were coordinated with the EHT campaign. We reduced the data using the NuSTAR Data Analysis Software NuSTARDAS-v.1.6.0<sup>11</sup> and HEASOFT-v.6.19, filtered for periods of high instrumental background due to South Atlantic Anomaly (SAA) passages and known bad detector pixels. Photon arrival times were corrected for on-board clock drift and processed to the Solar System barycenter using the JPL-DE200 ephemeris. We used a source extraction region with  $50''$  radius centered on the radio position of Sgr A\* and extracted 3–79 keV light curves in 100 s bins with deadtime, PSF, and vignetting effects corrected (see Zhang et al. 2017a, for further details on NuSTAR

<sup>9</sup> <https://heasarc.gsfc.nasa.gov/lheasoft/>

<sup>10</sup> Chandra Interactive Analysis of Observations (CIAO) is available at <http://cxc.harvard.edu/ciao/>.

<sup>11</sup> <https://heasarc.gsfc.nasa.gov/docs/nustar/analysis>.

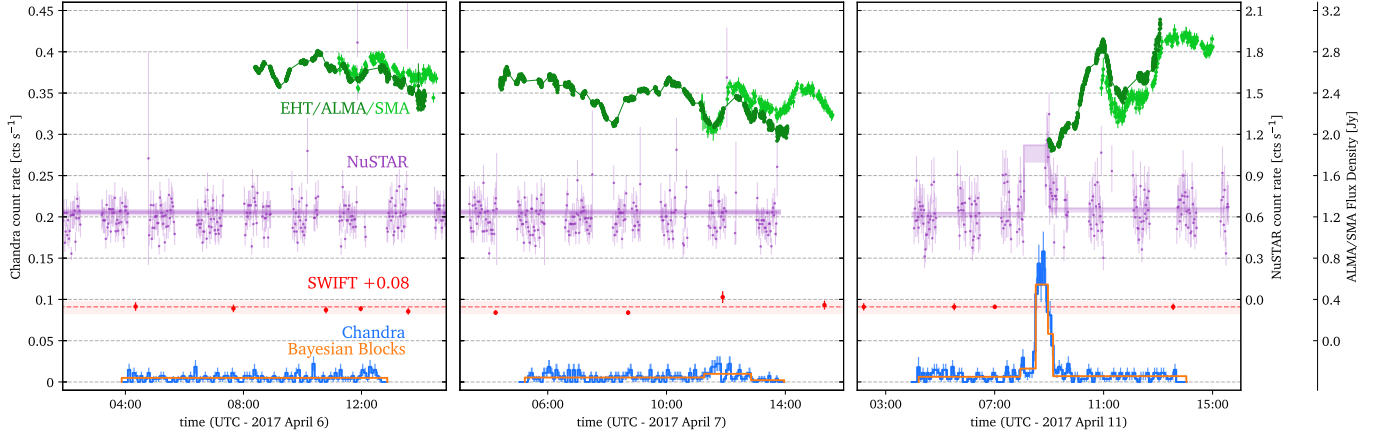


**Figure 4.** Light curves from ALMA and SMA between 213 – 229 GHz (dark and light green points, respectively; see Wielgus et al. 2022, for details), along with (quasi-)simultaneous, coordinated Swift (red; 2–10 keV), Chandra (blue; 2–8 keV), and NuSTAR (purple; 3–79 keV) observations on 2017 April 6, 7, and 11. The long term average flux value of Sgr A\* measured from Swift is plotted as a red dashed line with upper and lower  $2\sigma$  percentiles for the 2017 cumulative flux distribution marked with a light red shaded region (e.g., Degenaar et al. 2013b, 2015). The Bayesian block flare detection algorithm (Scargle 1998; Scargle et al. 2013; Williams et al. 2017) has been run on the Chandra and NuSTAR light curves and results, including flare detections on 7 and 11 April, are over-plotted as orange histograms on the Chandra data and purple histograms on the NuSTAR data.

Sgr A\* data reduction). For all three observations we made use of the data obtained by both focal plane modules FPMA and FPMB.

For flare spectral analysis, we used `nuproducts` in HEASOFT-v.6.19 to create spectra and responses from  $30''$  circular regions (as recommended for faint sources to minimize the background) centered on the coordinates of Sgr A\*. As explained in 4.2.4, NuSTAR only partially detected a flare from Sgr A\* on 2017 April 11 (observation ID 30302006004), hence we focus on this observation alone in the present work. The source spectrum was extracted from the NuSTAR Good Time Intervals (GTIS) that overlaps with the Chandra flare duration. The background spectrum was extracted from off-flare time intervals in the same observation.

#### 4.2.4. X-ray Flare Spectral Analysis

To obtain the best constraint on the spectrum of Sgr A\* during its faint and moderate X-ray flares, we performed joint Chandra/NuSTAR spectral analysis of the two flares described in Section 4.2.2. The following analysis was performed in ISIS v1.6.2-43 and made use of Remeis `isisscripts`<sup>12</sup>. Chandra flare spectra were binned to a minimum of four channels and a  $S/N$  ratio of 3 above 0.5 keV while off-flare spectra were combined and binned to a minimum of two channels and  $S/N$  of 3; we fit bins contained within the interval 1–9 keV. The NuSTAR FPMA/FPMB spectra of the 2017 April 11 flare were binned to a combined minimum  $S/N$  of 2 and

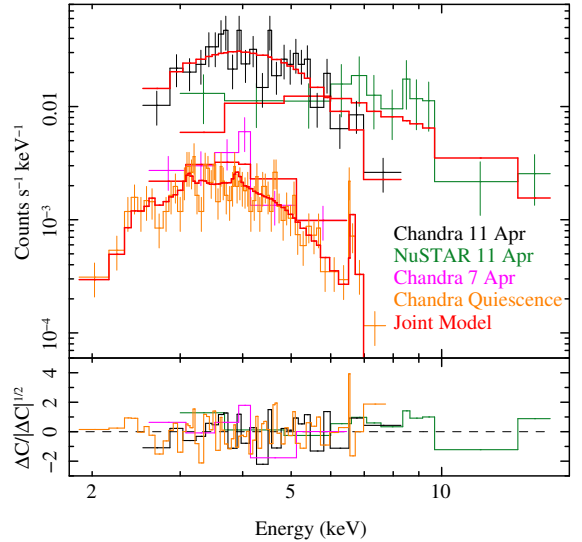


**Figure 5.** Joint Chandra-NuSTAR spectra of flares from Sgr A\*. The magenta and black spectra are the Chandra flare spectra from 2017 April 7 and 2017 April 11, respectively; the 2017 April 11 NuSTAR FPMA and FPMB flare spectra are combined for plotting purposes and shown in green. The orange data are the combined spectrum from the off-flare quiescent intervals of all four Chandra observations. The model described in Section 4.2.4 is shown in red for each dataset.

a minimum of three channels above 3 keV. We ignored all bins not fully contained within the interval 3–79 keV.

Given the relatively small numbers of counts, we opted for simple absorbed power law models for the flare

<sup>12</sup> This research has made use of a collection of ISIS functions (ISISScripts) provided by ECAP/Remeis observatory and MIT (<http://www.sternwarte.uni-erlangen.de/isis>)

spectra and we compared our model to our data with Cash statistics (Cash 1979). We used the **TBvarabs** model with Wilms abundances and Verner cross-sections (Verner et al. 1996; Wilms et al. 2000) and assumed a shared spectral index for both flares. (There is no conclusive evidence for a relationship between X-ray flare luminosity and X-ray spectral index; Neilsen et al. 2013a; Zhang et al. 2017b; Haggard et al. 2019.) Because a portion of the 2017 April 11 flare fell within a gap in the NuSTAR light curve, we included a cross-normalization constant between our NuSTAR and Chandra spectra (as well as between the FPMA and FPMB spectra).

For NuSTAR, we simply defined the spectrum of the off-flare interval as the background file for the 2017 April 11 flare spectrum, but we had to treat the Chandra spectra differently because they are susceptible to pileup during flares (e.g., Nowak et al. 2012a), though fainter flares like those described here are not likely to be impacted. In particular, because pileup depends on the total count rate, not the background count rate, it is necessary to model the background spectrum and treat the flare emission as the sum of the background model and the absorbed power law. We fit the quiescent (off-flare) emission with a single **vapec** model; see Nowak et al. (2012a) for more details.

Once we had a satisfactory fit to the joint flare spectra, we used the **emcee** Markov Chain Monte Carlo (MCMC) routine to find credible intervals for our fit parameters. For our MCMC runs, we used 10 walkers (i.e., 10 members of the ensemble) for each of our 10 free parameters, and allowed them to evolve for 10,000 steps (a total of 1 million samples). These runs appear to converge within the first several tens of steps, so we discard the first 500 steps. We estimate an autocorrelation time for our parameter chains between  $\sim 200$  and 400 steps, indicating that we have 2500–5000 independent samples of each parameter.

Finally, we calculate the minimum width 90% credible interval for each parameter. We compute the cumulative distribution function for the samples for each parameter and select the smallest interval that contains 90% of the samples. The results are given in Table 3. Sgr A\* flares are highly absorbed, with a column density of  $N_{\text{H}} = 17.8^{+3.5}_{-2.5} \text{ cm}^{-2}$ ; this is a bit higher than the values found by Nowak et al. (2012a) and Wang et al. (2013), but the differences are within  $1\text{-}\sigma$  in both cases. The photon index of the flare is  $\Gamma = 2.1^{+0.5}_{-0.4}$ , which is not well constrained but is consistent with other analyses of X-ray flares (Porquet et al. 2008; Nowak et al. 2012a; Neilsen et al. 2013b; Haggard et al. 2019). The 2017 April 7 flare is only detected at 99% confidence, but has an unabsorbed 2–10 keV flux of  $F_{0704,2-10} = (0.3 \pm 0.2 \times 10^{-12}) \text{ erg s}^{-1} \text{ cm}^{-2}$  and a 3–79 keV flux  $F_{0704,3-79} = (0.5^{+0.8}_{-0.4}) \times 10^{-12} \text{ erg s}^{-1} \text{ cm}^{-2}$ . The 2017 April 11 flare has an unabsorbed 2–10 keV flux of  $F_{1104,2-10} = (7.8^{+2.6}_{-3.9}) \times 10^{-12} \text{ erg s}^{-1} \text{ cm}^{-2}$ , which

**Table 3.** Chandra/NuSTAR Joint Spectral Parameters

Parameter	Value	Units
$N_{\text{H}}$	$17.8^{+3.5}_{-2.5}$	$10^{22} \text{ cm}^{-2}$
$\Gamma$	$2.1^{+0.5}_{-0.4}$	...
$N_{\text{FPMB}}$	$1.2^{+0.9}_{-0.4}$	...
$K_{\text{vapec}}$	$0.0012^{+0.0009}_{-0.0005}$	...
$kT_{\text{vapec}}$	$2^{+0.4}_{-0.5}$	keV
$N_{\text{ACIS}}$	$1^{+0.7}_{-0.3}$	...
$F_{0704,2-10}$	$0.3^{+0.2}_{-0.2}$	$10^{-12} \text{ erg s}^{-1} \text{ cm}^{-2}$
$F_{0704,3-79}$	$0.5^{+0.8}_{-0.4}$	$10^{-12} \text{ erg s}^{-1} \text{ cm}^{-2}$
$F_{1104,2-10}$	$7.8^{+2.6}_{-3.9}$	$10^{-12} \text{ erg s}^{-1} \text{ cm}^{-2}$
$F_{1104,3-79}$	$15.4^{+8.9}_{-7.5}$	$10^{-12} \text{ erg s}^{-1} \text{ cm}^{-2}$
$F_{\text{Q},2-10}$	$0.5^{+0.2}_{-0.1}$	$10^{-12} \text{ erg s}^{-1} \text{ cm}^{-2}$
$F_{\text{Q},3-79}$	$0.31^{+0.05}_{-0.03}$	$10^{-12} \text{ erg s}^{-1} \text{ cm}^{-2}$

NOTE— $N_{\text{H}}$  is the X-ray absorbing column density.

$\Gamma$  is the flare photon index.  $N_{\text{FPMB}}$  is the cross-normalization of the NuSTAR FPMB relative to the FPMA.  $K_{\text{vapec}}$  and  $kT_{\text{vapec}}$  are the normalization and temperature of the quiescent **vapec** component.  $N_{\text{ACIS}}$  is the cross-normalization of the Chandra ACIS spectrum relative to NuSTAR. Flare ( $F_{0704}$ ,  $F_{1104}$ ) and quiescent fluxes ( $F_{\text{Q}}$ ) are quoted for the intervals 2–10 keV and 3–79 keV — the X-ray quiescent and flare fluxes presented in Table 2 are  $\nu F_{\nu}$  in units of  $\text{erg s}^{-1} \text{ cm}^{-2}$ , and so differ slightly from the integrated values quoted here. See §4.2.4 and §5.2.2 for further details.

rises to  $F_{1104,3-79} = (15.4^{+8.9}_{-7.5}) \times 10^{-12} \text{ erg s}^{-1} \text{ cm}^{-2}$  over the interval 3–79 keV.

As reported in Neilsen et al. (2015), the quiescent X-ray flux ( $F_{\text{Q},2-10}$ ) results from an admixture of two components. At the faint end of Sgr A\*'s flux distribution, there are both variable and steady components, with the variable component likely arising from unresolved faint flares which contribute  $\sim 10\%$  of the apparent quiescent flux (see also Neilsen et al. 2013c). Adopting the 2–10 keV flux from this joint fit (Table 3) and allowing a generous  $\sim 1/3$  contribution from unresolved X-ray flares, we estimate an upper limit on the median luminosity of  $\sim 10^{33} \text{ erg s}^{-1}$ . Larger flare contributions would be inconsistent with estimates that approximately 90% of the quiescent emission from Sgr A\* is in fact associated with spatially resolved emission.

## 5. FINAL DATA PRODUCTS

### 5.1. Event Horizon Telescope Data Products

In this section, we describe the properties of the 2017 Sgr A\* EHT VLBI data. In particular, we detail the  $(u, v)$ -coverage, correlated flux densities, systematic error budgets, estimations for residual antenna-based gain errors, the influence of interstellar scattering on the measured visibilities, conservative estimates for the size of Sgr A\* at 1.3 mm, and an assessment of the source variability.

#### 5.1.1. Data content

The observing schedules and  $(u, v)$ -coverages of our April 6 and 7 Sgr A\* observing days are shown in [Figure 1](#) and [Figure 6](#), respectively. Correlated flux densities as a function of baseline length are shown in [Figure 7](#). The measurements show a good agreement between the products of our processing pipelines. The amplitude data presented in [Figure 7](#) are broadly consistent with the Fourier signature of a blurred ring, indicating the presence of two minima at  $\sim 3$  G $\lambda$  and  $\sim 6.5$  G $\lambda$ .

The calibrated Stokes  $\mathcal{I}$  VLBI data of Sgr A\* are made publicly available through the EHT data portal<sup>13</sup> under the 2022-DXX-XX code.

#### 5.1.2. Systematic error budget

We compute  $S/N > 7$  closure phases ( $\psi_C$ ) and log closure amplitudes ( $\ln A_C$ ), which are reasonably well described by a normal distribution ([Blackburn et al. 2020](#)), to estimate the amount of systematic noise  $s$  present in the EHT data following [M87\\* Paper III](#) and [Wielgus et al. \(2019\)](#). We have augmented these “traditional” closure phases and closure amplitude tests with novel closure trace quantities,  $\mathcal{T}$ , described in [Broderick & Pesce \(2020\)](#). Closure traces are complex composite data structures, which we characterize by their phase and log amplitude. The closure traces are produced from parallel- and cross-hand correlation products, and they are insensitive to all linear station-based corruptions of the data, including both station gains and polarization leakage. The uncertainty  $\sigma_x$  of a data product  $X$  follows from the a priori estimated thermal noise  $\sigma_{\text{th}}$  from our calibration pipelines and a constant systematic non-closing error  $s_x$  as

$$\sigma_x^2 = \sigma_{\text{th}}^2 + s_x^2. \quad (3)$$

We estimate  $s_x$  based on the criterion that the median absolute deviation of  $X/\sigma_x$  becomes unity for the following data quantities:

1. RR – LL closure phases ( $X = \psi_{C, \text{RR}} - \psi_{C, \text{LL}}$ ) and log closure amplitudes ( $X = \ln A_{C, \text{RR}} - \ln A_{C, \text{LL}}$ ), which should be zero in the absence of significant circular source polarization and instrumental polarization leakage.

2. Low-band – high-band closure phases ( $X = \psi_{C, \text{lo}} - \psi_{C, \text{hi}}$ ), log closure amplitudes ( $X = \ln A_{C, \text{lo}} - \ln A_{C, \text{hi}}$ ), closure trace phases ( $X = \arg(\mathcal{T}_{\text{lo}}) - \arg(\mathcal{T}_{\text{hi}})$ ), and log closure trace amplitudes ( $X = \ln |\mathcal{T}_{\text{lo}}| - \ln |\mathcal{T}_{\text{hi}}|$ ), all of which should be close to zero in the absence of significant variations of source structure and flux over the observed EHT bandwidth. The phase shift due to the small frequency difference between the two bands is negligible.
3. Closure phases of small, trivial triangles ( $X = \psi_{C, \text{trivial}}$ ) and log closure amplitudes of small, trivial quadrangles ( $X = \ln A_{C, \text{trivial}}$ ), which should be zero in the absence of significant instrumental polarization leakage as they probe the symmetric large-scale source structure. Additionally, trivial closure phases will be affected by large-scale source structures.
4. Closure trace phases ( $X = \arg(\mathcal{T}_{\text{trivial}})$ ) and closure trace log amplitudes ( $X = \ln |\mathcal{T}_{\text{trivial}}|$ ) on trivial boomerang quadrangles, in which a site is repeated so that the area of the quadrangle vanishes. Both sets of quantities should be zero in the absence of nonlinear station-based or baseline-based errors.

To avoid biases in the closure trace log amplitudes arising from low  $S/N$ , we construct all closure quantities  $X$  from visibilities that have been coherently averaged over 120 s and apply the same  $S/N > 7$  threshold; we subsequently average the constructed closure traces on scan-length intervals. We note that these averaging timescales carry with them the potential for decoherence losses resulting from atmospheric delays and/or structural variability.

The systematic error budgets derived for Sgr A\*, NRAO 530, and J1924–2914 are shown in [Table 4](#). These are estimated using only data on days when ALMA was observing, i.e., 2017 April 6, 7, and 11. However, we exclude Sgr A\* data from 2017 April 11 due to flaring activity – these will be the subject of a forthcoming study (see also [Wielgus et al. 2022](#)). The underlying distributions of the various data quantities, with and without added systematic error, are shown in [Figure 8](#).

From the combined data on all baselines, an excess in systematic errors of RR – LL closure quantities can be seen for Sgr A\* compared to the observed NRAO 530 and J1924–291 calibrator sources. These offsets may be indicative of intrinsic source polarization in Sgr A\*. However, the overall offsets are just at the level of thermal noise for scan-averaged data. It is likely for source polarization to be significant on particular baselines only. Horizon-scale polarization signatures in the 2017 Sgr A\* EHT data will be analyzed in future work.

The systematic error budgets agree between the traditional closure quantities and the novel closure traces.

<sup>13</sup> <https://eventhorizontelescope.org/for-astronomers/data>.



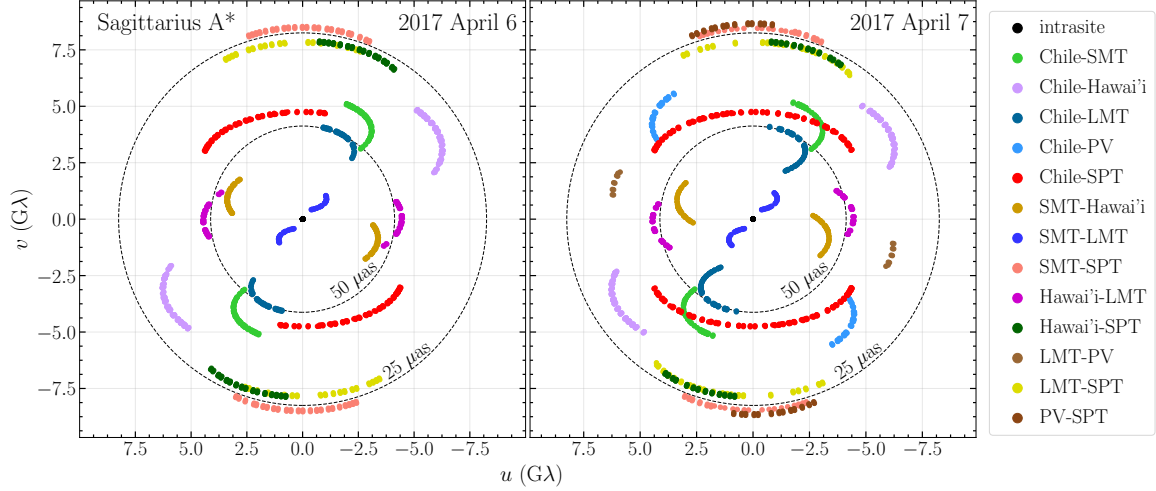


**Figure 6.**  $(u, v)$ -coverages from fringe detections of Sgr A\* on 2017 April 6 and 7 plotted from scan-averaged data. Fringe spacings of 25 and 50  $\mu\text{as}$  are indicated with dashed circles.

It is therefore unlikely for large-scale source structure and uncorrected polarization leakage effects to be the dominant sources of systematic uncertainties.

There are several EHT data issues affecting Sgr A\* observations that require special care. These are described in detail in M87\* Paper III and briefly summarized below.

1. The JCMT and SMA used an identical frequency setup derived from a shared frequency standard in 2017. Radio-frequency interference (RFI) is not washed out due to low fringe rate. Both stations are therefore never chosen as the reference station for the correction of atmospheric phase fluctuations. Resultant amplitude errors on this baseline are mostly mitigated by flagging channels affected by RFI and network calibration.
2. An instability in the maser used in 2017 for PV caused a de-correlation over the 0.4s correlator accumulation period, which was corrected by up-scaling the SEFD.
3. Partial data dropouts due to a misconfigured Mark 6 recorder at APEX have been accounted for by adjusting the amplitudes and data weights accordingly during correlation. A hard drive failure at the JCMT, causing 1/16th of the low band data to be lost, has been similarly corrected. Furthermore, a small SEFD correction factor has been applied to the APEX data to correct for an amplitude loss from an interfering 1 pulse-per-second signal.
4. High band SMA SEFDs on the first three observing days have been up-scaled to correct for occasionally corrupted frequency channels in the beam-former system.

5. A negligible  $< 0.1\%$  amplitude loss due to a periodic ALMA correlator glitch occurring every 18.192s was left uncorrected. Moreover, a baseline-dependent  $\sim 0.67\%$  signal loss due to finite fast-Fourier-transform lengths over the full 2048 MHz band on non-ALMA baselines has not been corrected.

The systematic error studies presented in Figure 8 and Table 4 reflect a comparable level of data quality and internal self-consistency for the CASA and HOPS data products. All data distributions are well behaved and the different amounts of estimated systematic noise are balanced, being sometimes higher in one or the other data set. Small differences in the number of recorded visibilities are due to the effects of thresholding near the detection limit as well as slight differences in flagging between the two pipelines.

As indicated also by the scatter in the  $s$  measurements, optimal systematic error budgets depend on the exact baselines and data quantities used. A crude recommendation for data averaged in 120s bins is to adopt  $2.5^\circ$  for closure phases and 9% for log closure amplitudes.

### 5.1.3. Gain errors

Ensembles of opacity-corrected antenna temperature ( $T_a^*$ ) measurements are used to fit for gain curves and DPFUs (Janssen et al. 2019a; Issaoun et al. 2017). For the gain curve, we fit

$$gc(E) = 1 - B(E - E_0)^2, \quad (4)$$

to normalized  $T_a^*$  values from quasars tracked over a wide range of elevations  $E$ . The parameters  $B$  and  $E_0$  describe the peak and shape of the gain curve, respectively. For the DPFU, we typically fit a constant value

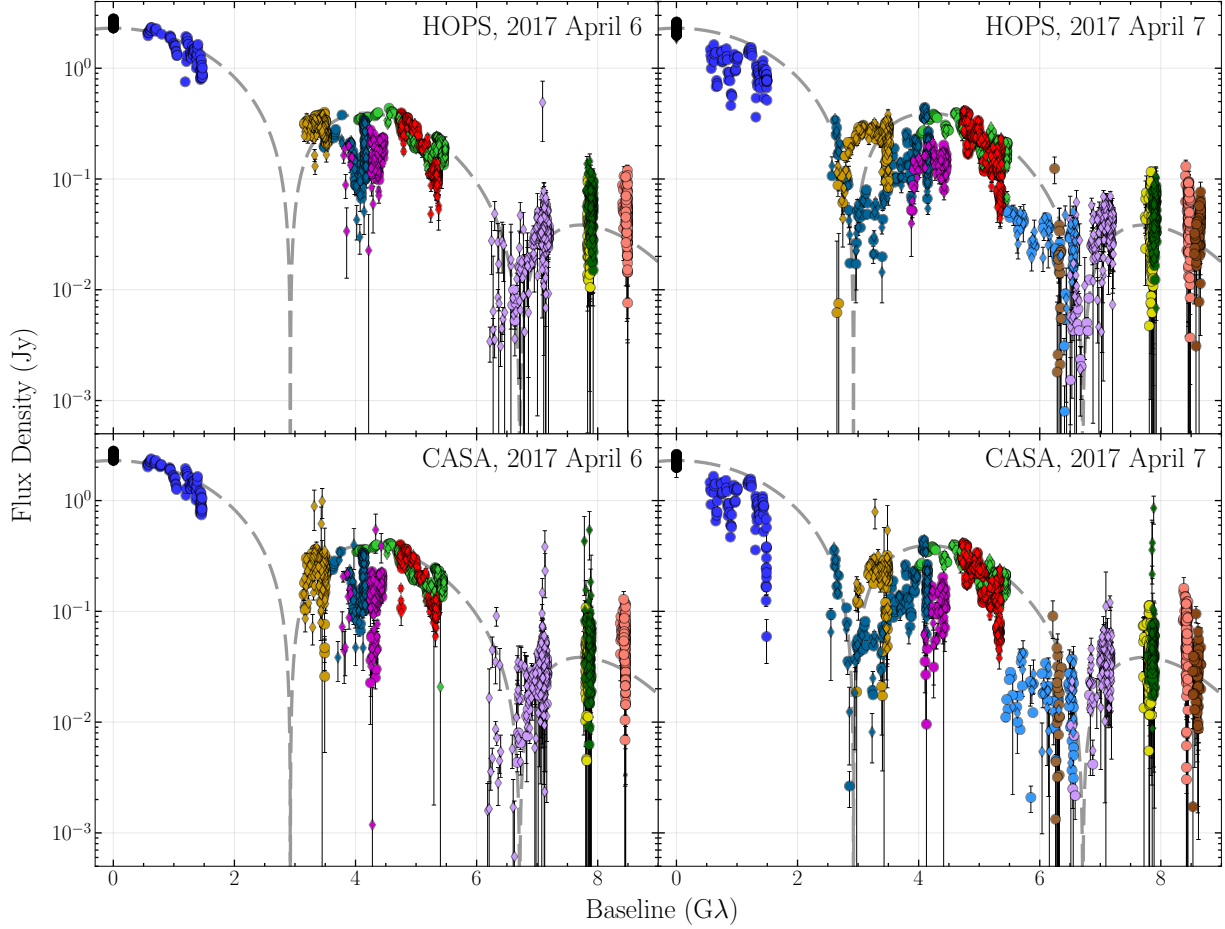


**Figure 7.** Measured correlated flux densities of Sgr A\* on April 6 and 7 of the HOPS (top panel) and CASA (bottom panel) data overplotted with a thin (unresolved) ring model with a  $\sim 50 \mu\text{s}$  diameter, that has been blurred with a  $23 \mu\text{s}$  FWHM circular Gaussian source (Paper III; Paper IV). Flux densities have been calibrated based on estimated station SEFDs, measured light curves (Section 3.2.1), and calibrator gain transfers (Section 5.1.3). The data are averaged in 120 s bins, which causes phase coherence losses in a few scans. Error bars denote  $\pm 1\sigma$  uncertainty from thermal noise. Detections are color-coded by baselines, as in Figure 6. Redundant baselines are shown with different symbols: circles for baselines to ALMA and SMA; diamonds for baselines to APEX and JCMT.

for the entire observing track to  $T_a^*$  measurements of solar system objects to estimate the constant aperture efficiency  $\eta_{\text{ap}}$ . A statistical  $T_a^*$  scatter translates into uncertainties of the fitted  $B$ ,  $E_0$ , and  $\eta_{\text{ap}}$  parameters of the gain curve and DPFU, respectively. The uncertainty of the planet model brightness temperature is added in quadrature for the DPFU fitting. For the Butler (2012) models, we have a 10 % uncertainty for Saturn and 5 % for Mars, Jupiter, and Uranus. The error contribution from  $T_{\text{sys}}^*$  measurements is negligible. Finally, ALMA and SMA exhibit an additional calibration uncertainty from the phasing efficiency. The performance of ALMA has been determined in the quality assurance stage 2 (QA2) ALMA interferometric reduction of data (Goddi et al. 2019). The final calibration method is described in Section 3.2.1, for which we have estimated a global 10 % flux density calibration uncertainty. The small SMA dishes are well characterized. Here, the phasing

efficiency dominates the overall calibration uncertainty, which ranges between 5 % in optimal observing conditions and 15 % when the phasing efficiency is low. The a priori flux calibration parameters are summarized in Table 5. The reported uncertainties provide a good upper limit for residual gain errors. Compared to our 2017 M87\* data (M87\* Paper III), the DPFU values are slightly updated, which does not affect our previous results, while the gain curves stayed the same.

However, there are several loss factors that are not captured in our a priori calibration framework, most notably imperfect pointing and focus solutions of individual telescopes. The case is most severe for the large LMT dish, where the measured DPFU varies from day to day. In order to provide a conservative estimate of the gain uncertainties, a bootstrap approach was applied to the DPFU measurements on 2017 April 6 and 7. With 10000 medians drawn from the bootstrapped

**Table 4.** Non-closing systematic uncertainties,  $s$  (and in units of thermal noise,  $s/\sigma_{\text{th}}$ ), for Sgr A\* and its calibrators estimated using various statistical tests on both the CASA and HOPS products. The data from April 6 and 7 have been used for Sgr A\*, and for the calibrators, we have also used April 11.  $n$  is the number of closure quantities used for each test.

Source	Test	CASA			HOPS		
		$s$	$s/\sigma_{\text{th}}$	$n$	$s$	$s/\sigma_{\text{th}}$	$n$
Sgr A*	RR – LL closure phases	3.6°	0.6	313	3.6°	0.6	328
	lo – hi closure phases	2.1°	0.3	333	2.0°	0.3	367
	trivial closure phases	0.2°	0.1	373	1.0°	0.2	411
	RR – LL log closure amplitudes	10.9%	0.8	239	11.3%	0.9	278
	lo – hi log closure amplitudes	9.7%	0.6	284	7.6%	0.5	371
	trivial log closure amplitudes	5.6%	0.5	168	1.4%	0.1	212
	lo – hi closure trace phases	1.1°	0.2	97	0.0°	0.0	125
	trivial closure trace phases	1.5°	0.3	160	0.0°	0.0	158
	lo – hi log closure trace amplitudes	3.7%	0.4	97	0.0%	0.0	125
	trivial log closure trace amplitudes	5.7%	0.6	160	4.6%	0.5	158
NRAO 530	RR – LL closure phases	1.4°	0.2	125	0.0°	0.0	121
	lo – hi closure phases	2.5°	0.3	156	2.8°	0.3	150
	trivial closure phases	0.0°	0.0	151	0.0°	0.0	147
	RR – LL log closure amplitudes	0.4%	0.0	114	0.0%	0.0	117
	lo – hi log closure amplitudes	0.0%	0.0	203	2.7%	0.1	188
	trivial log closure amplitudes	6.2%	0.6	100	3.2%	0.3	91
	lo – hi closure trace phases	1.3°	0.2	56	0.0°	0.0	54
	trivial closure trace phases	0.0°	0.0	104	0.0°	0.0	95
	lo – hi log closure trace amplitudes	5.6%	0.5	56	8.5%	0.8	54
	trivial log closure trace amplitudes	2.1%	0.2	104	0.0%	0.0	95
J1924–2914	RR – LL closure phases	2.4°	0.5	207	2.6°	0.5	235
	lo – hi closure phases	1.1°	0.2	224	0.9°	0.2	280
	trivial closure phases	0.5°	0.2	190	0.0°	0.0	204
	RR – LL log closure amplitudes	2.0%	0.2	272	3.5%	0.3	313
	lo – hi log closure amplitudes	6.6%	0.6	367	6.8%	0.7	455
	trivial log closure amplitudes	3.7%	0.5	190	4.2%	0.6	218
	lo – hi closure trace phases	2.3°	0.5	222	1.3°	0.3	253
	trivial closure trace phases	2.2°	0.8	106	1.9°	0.7	106
	lo – hi log closure trace amplitudes	5.5%	0.7	222	6.4%	0.8	253
	trivial log closure trace amplitudes	0.0%	0.0	106	2.6%	0.5	106

samples, we are able to derive the Median Absolute Deviations, which is then scaled to an equivalent sigma. With this method we find a  $\sim 35\%$  uncertainty on the LMT DPFU.

Additionally, the antenna gains can be characterized by amplitude self-calibration, which solves the empirical corrections for time-variable instrumental or environmental factors that cannot be measured directly. In order to avoid any variability from Sgr A\* that could contaminate the antenna gain estimations, the scan-averaged visibility data of calibrators (J1924–2914 and

NRAO 530) are utilized by assuming their stationarity in both source structure and flux density. For both calibrators, the fiducial images independently produced with different imaging pipelines (i.e., eht-imaging, SMILL, Difmap and DMC; [Paper III](#); [Paper IV](#)) are employed to improve the statistics on the gains (for more details, see [Jorstad et al. \(2022\)](#); [Issaoun et al. \(2022\)](#)). We use the mean values of the gains obtained from each imaging pipeline. As an example, the resultant antenna gains derived by amplitude self-calibration for the low-band datasets for both calibrators are shown in [Figure 9](#).

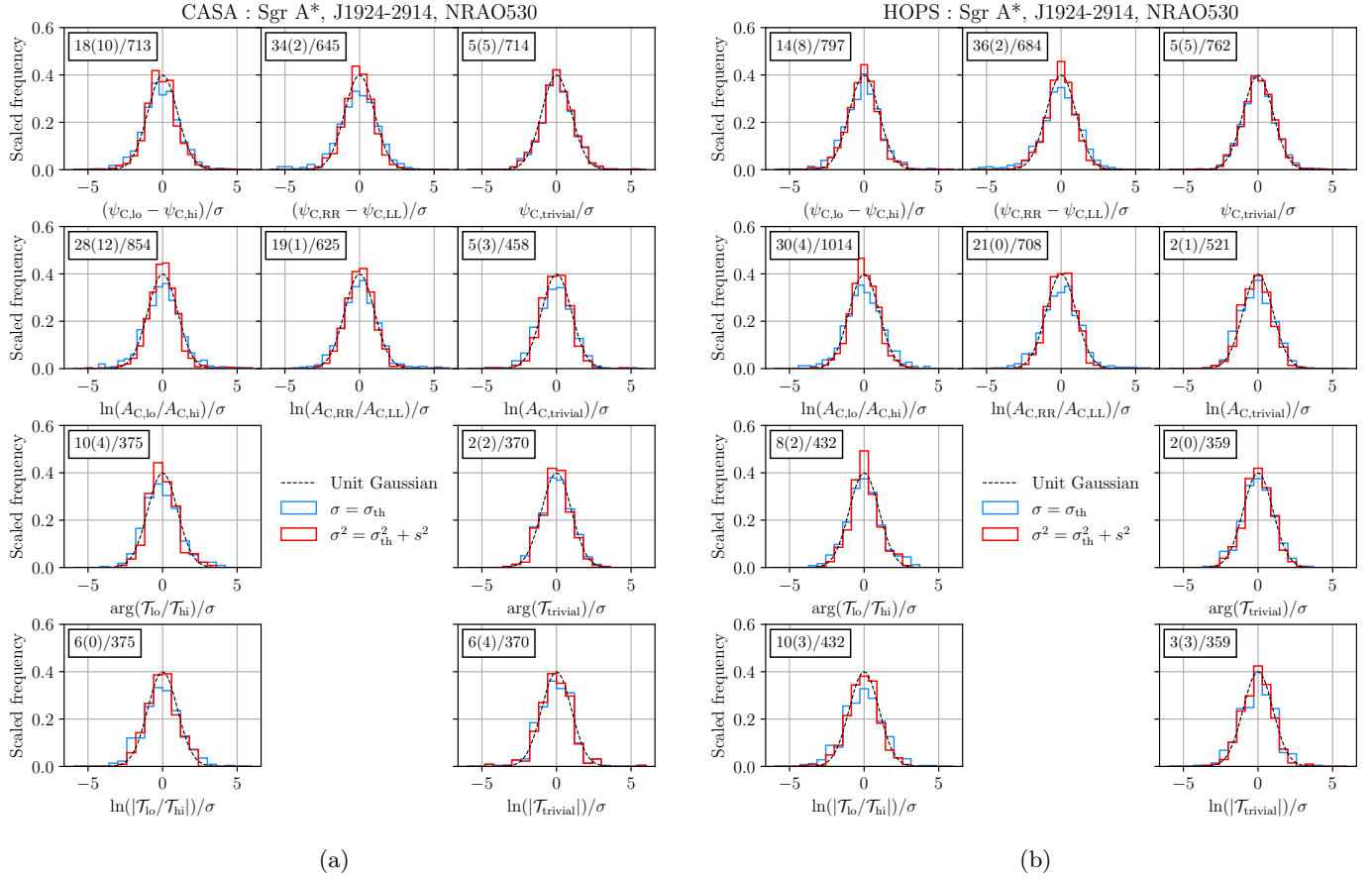


**Figure 8.** Normalized distributions of lo–hi, RR–LL and trivial closure quantities, as well as lo–hi and trivial closure trace quantities of Sgr A\*, NRAO 530, and J1924–2914 from both the CASA (a) and HOPS (b) reduction pipelines. The data from April 6 and 7 have been used for Sgr A\*, and for the calibrators, we have also used April 11. The distributions prior to (blue) and after (red) accounting for the estimated systematic uncertainties,  $s$ , are shown. The values of  $s$  for each source and reduction pipeline are given in Table 4. In the top left corner of each distribution, the number of  $> 3\sigma$  outliers are given considering thermal noise only followed by the number of outliers considering thermal plus systematic noise for  $\sigma$  in parenthesis. These numbers are followed by the total number of data points after a slash.

The results were obtained after performing a gain alignment procedure meant to minimize the offset between the gains from the two calibrators within the overlapping time and flagging the data points lying beyond  $3\sigma$  from the mean value. The procedure is as follows: (1) we first derive a mean gain value for each calibrator by only using the gains in the overlapping times; (2) from these gain mean values for the two calibrators, in the overlapping times, we derive an average gain value and re-scale the two calibrators’ mean gains with this average value; (3) the scaling factors thus obtained are then applied to the gains over the entire time range. The mean gains for each station (reported on top of each frame in Figure 9) are within their corresponding a priori DPFU error budgets (Table 5). We can therefore assume that the calibrator self-calibration method captures the known gain uncertainties that enter into our a priori flux density calibration error budget. At this point, we linearly interpolate the fiducial gains obtained

from the calibrators to the Sgr A\* timestamps and we apply them to the Sgr A\* data.

#### 5.1.4. Interstellar scattering

Interstellar scattering is a long-known extrinsic effect on the observed radio structure of Sgr A\* (Davies et al. 1976). The scattering of radio waves from Sgr A\* is predominantly caused by foreground stochastic turbulent electrons along the line of the sight located far from the Galactic Center (Bower et al. 2014a; Dexter et al. 2017). At long observing wavelengths, the most dominant effect on the source structure is angular broadening, a chromatic effect arising from diffractive scattering (see, e.g., Narayan 1992), resulting in a Gaussian image with a size proportional to the squared wavelength for wavelengths  $\lambda \gtrsim 1$  cm (Davies et al. 1976; van Langevelde et al. 1992; Bower et al. 2004b; Shen et al. 2005; Bower et al. 2006; Johnson et al. 2018b; Lu et al. 2018). Furthermore, the scattering is anisotropic, with stronger angular broaden-



**Table 5.** EHT flux density calibration parameters and their uncertainties. For phased arrays (ALMA and SMA), the DPFUs represent the combined sensitivity of all phased dishes. The gain curve parameters as a function of elevation  $E$  are given based on a  $gc(E) = 1 - B(E - E_0)^2$  parameterization (Equation 4).

Station(code)	RCP DPFU [K/Jy]	LCP DPFU [K/Jy]	$B$	$E_0$
ALMA(AA) <sup>a</sup>	$1.03 \pm 10\%$	$1.03 \pm 10\%$	0	0
APEX(AP)	$0.0245 \pm 11\%$	$0.0250 \pm 11\%$	$0.00002 \pm 3.6\%$	$36.6 \pm 1\%$
IRAM 30-m(PV) <sup>b</sup>	$0.034 \pm 10\%$	$0.033 \pm 10\%$	$0.00018 \pm 5.3\%$	$43.7 \pm 1.3\%$
JCMT(JC) <sup>c</sup>	$(0.026 \pm 14\%) - (0.033 \pm 11\%)$		0	0
LMT(LM) <sup>d</sup>	$0.061 \pm 35\%$	$0.064 \pm 35\%$	0	0
SMA(SM) <sup>e</sup>	$0.046 \pm (5 - 15)\%$	$0.046 \pm (5 - 15)\%$	0	0
SMT(AZ)	$0.01683 \pm 7\%$	$0.01681 \pm 7\%$	$0.000082 \pm 10.4\%$	$57.6 \pm 2.0\%$
SPT(SP) <sup>f</sup>	$0.0061 \pm 15\%$	$0.0061 \pm 15\%$	0	0

<sup>a</sup>The ALMA DPFU uncertainty is based on the overall 10% uncertainty estimated by the QA2 team.

<sup>b</sup>The PV DPFU has been scaled down by a factor of 3.663 to account for the known maser instability in 2017.

<sup>c</sup>For the JCMT DPFU, a range between the smallest daytime value and the nighttime value is given.

<sup>d</sup>The LMT has an unparametrized 10% uncertainty on the gain curve, which has been added to the DPFU uncertainty. The DPFU values shown here are from 2017 April 7. The uncertainty is the most conservative value from April 6.

<sup>e</sup>The SMA DPFU uncertainty is based on the dominant 5-15% uncertainty on the phasing efficiency.

<sup>f</sup>The gain curve of the SPT is uncharacterized, as normalized antenna temperature values cannot be obtained from sources that remain at a constant elevation when observed from the South Pole.

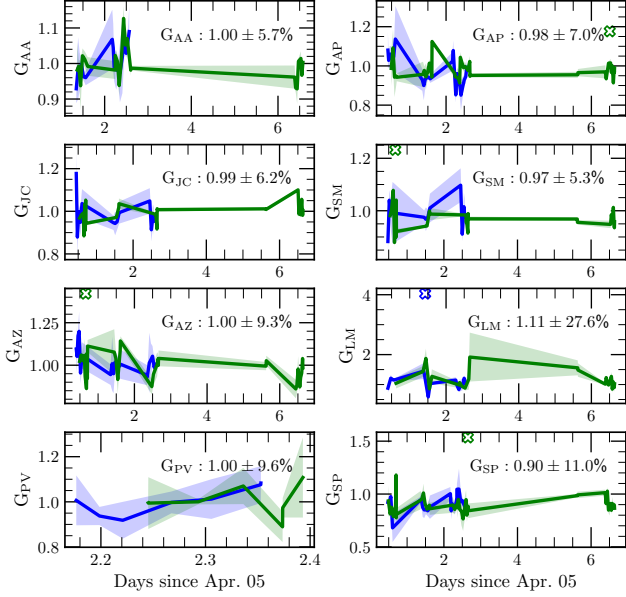


**Figure 9.** Low-band antenna gains of NRAO 530 (blue curve) and J1924–2914 (green curve) by amplitude self-calibration. The two-letter station codes are taken from Table 5. The colored bands indicate  $1\sigma$  uncertainties of the gains. The empty cross symbols represent the flagged data points lying beyond  $3\sigma$  from the mean value. The PV telescope observed Sgr A\* only on April 7.

ing along the east-west direction compared to the north-south direction (Frail et al. 1994; Jauncey et al. 1989). The angular broadening has a full width at half maximum (FWHM) of  $(1.380 \pm 0.013)\lambda_{\text{cm}}^2$  mas along the major axis and  $(0.703 \pm 0.013)\lambda_{\text{cm}}^2$  mas along the minor axis, with the major axis at a position angle  $81.9^\circ \pm 0.2^\circ$  east

of north (Johnson et al. 2018a). The intrinsic source angular size is also chromatic, with a  $\theta_{\text{src}} \propto \lambda$  dependence (Johnson et al. 2018a). Consequently, observations at 1.3 mm, where historical measurements of Sgr A\* determined the size to be  $\sim 50\text{--}60\mu\text{as}$  (Doeleman et al. 2008; Fish et al. 2011; Lu et al. 2018; Johnson et al. 2018a), are in the regime where the intrinsic source structure is no longer sub-dominant to scattering and becomes the dominant structure in the image. Angular broadening can be described by a convolution of an unscattered image with a scattering kernel, or equivalently by a multiplication of the un-scattered, intrinsic interferometric visibilities by the appropriate Fourier-conjugate kernel (Goodman & Narayan 1989). More background information and reviews on interstellar scattering can be found in Rickett (1990), Narayan (1992), and Thompson et al. (2017).

Secondary effects arise from density irregularities in the interstellar medium, causing stochastic variations in the scattering, as well as diffraction effects. These variations introduce substructure in the image that is not intrinsic to the source (Goodman & Narayan 1989; Johnson & Gwinn 2015; Johnson & Narayan 2016; Psaltis et al. 2018). Scattering-induced substructure was first discovered in images of Sgr A\* at 1.3 cm by Gwinn et al. (2014) and later observed at other wavelengths (Johnson et al. 2018a; Issaoun et al. 2019b, 2021; Cho et al. 2022), giving additional constraints on the scattering properties of Sgr A\*. This substructure is caused by modes in the scattering material on scales comparable to the image extent, so scattering models with identical scatter-broadening may still exhibit strong differences in their scattering substructure. The substructure manifests in the visibility domain as “refractive noise”, which is an additive complex noise component with broad cor-

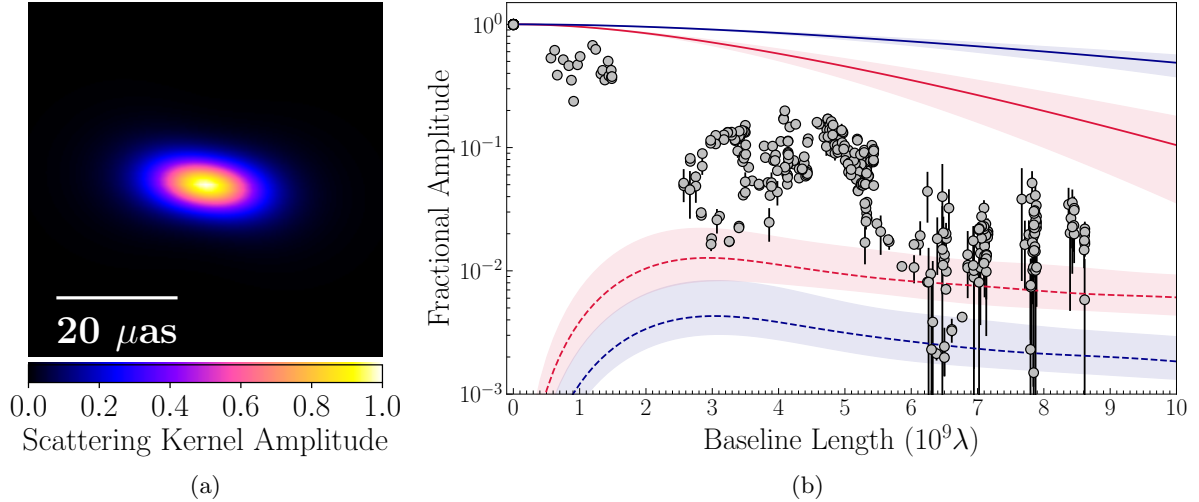


**Figure 10.** Diffractive scattering kernel and refractive noise rms at 1.3 mm based on the scattering model of Psaltis et al. (2018) and Johnson et al. (2018a). (a) The image-domain representation of the kernel, with a second moment of  $23.6 \times 12.1 \mu\text{as}$  in FWHM at  $\text{PA}=82^\circ$ . (b) The normalized kernel amplitude and refractive noise level at 1.3 mm as a function of the baseline length (lines), overlaid on normalized Sgr A\* low band data from 2017 April 7 (dots). The red and blue solid lines show the amplitudes of the kernel along the major and minor axes, respectively. The dashed lines show the rms refractive noise levels for a reference model in Paper III along each axis colored in the same way. The shaded area around each line covers the range of possible amplitude values given the uncertainties of scattering parameters in the model. The Sgr A\* amplitudes exhibit a steeper fall-off than that of the scatter-broadening kernel, indicative of resolved dominant intrinsic structure larger than the scattering kernel size. Furthermore, most of amplitudes are well above the expected range of the refractive noise, implying that the refractive substructure is likely not dominant in the observed structure. The most affected baselines are Chile to Hawai'i and Spain, Mexico to Spain and the South Pole, and Hawai'i to the South Pole, in the 6–8 G $\lambda$  range.

relation structure across baselines and time (Johnson & Narayan 2016). Using observations of Sgr A\* from 1.3 mm to 30 cm, Johnson et al. (2018a) have shown that the combined image broadening and substructure strongly constrain the power spectrum of density fluctuations, which is consistent with later observations that occurred close to the 2017 EHT observations of Sgr A\* described in this work (Sections 4.1.1 and 4.1.2) and in Issaoun et al. (2019b, 2021) and Cho et al. (2022).

Calibrated EHT data sets indicate that the intrinsic structure is dominant in measured visibilities, and that both diffractive and refractive scattering effects are limited, as anticipated from the empirically obtained scattering model and early EHT observations. In Figure 10, we show the scattering kernel in both the image and visibility domains based on the scattering parameters in Johnson et al. (2018a), together with the calibrated EHT data. The analysis from Johnson et al. (2018a) implies a non-Gaussian kernel (solid lines) more compact than the conventional Gaussian kernel adopted in early literature. Consequently, the angular broadening effect, i.e., multiplication of the intrinsic visibilities with the Fourier-conjugate kernel of scattering, causes a slight decrease in visibility amplitudes (and therefore the signal-to-noise ratio) by a factor of a few at maximum. The observed Sgr A\* visibility amplitudes exhibit a steeper decrease with baseline length than the scattering kernel, suggesting that the intrinsic source structure, larger

than the scattering kernel, is clearly resolved despite angular broadening.

The refractive substructure is likely also not dominant in Sgr A\* at 1.3 mm. In Figure 10 (b), we show typical refractive substructures along with the major and minor axes of the anisotropic scattering kernel expected for a reference model, adopted in Paper III, computed with `eht-imaging` based on the Psaltis et al. (2018) and Johnson et al. (2018a) scattering model (see Paper III Section 4.1 for details). While the rms noise levels due to the refractive substructure are dependent on the source size and shape (see, e.g., Johnson & Narayan 2016), the variations due to the deviation of the intrinsic source structure from the reference model are expected to be within a factor of a few (Paper III). Consequently, the effects of the refractive structure remains only a few percent of the total flux density at the maximum regardless of the source structure, hardly affecting the measured visibilities except for data points around the second null and/or at baselines longer than  $\sim 6 \text{ G}\lambda$ , which are in the low  $S/N$  regime. A more detailed analysis of the scattering properties on the observed visibilities and source structure is provided in Paper III. For the purposes of the current paper, we conclude that an estimate of the size of Sgr A\* drawn from visibility data will be dominated by the intrinsic structure of the source rather than scattering.

### 5.1.5. Source size and fractional compact flux density

The 1.3 mm source structure of Sgr A\* has been reported to have FWHMs of several tens of microarcseconds from early EHT observations in the last decade (Doeleman et al. 2008; Fish et al. 2011; Johnson et al. 2015; Lu et al. 2018), consistent with our 2017 observations (Figure 6). The SMT–LMT baseline is the shortest inter-site VLBI baseline provided in EHT observations, covering  $\sim 0.6$ – $1.5$  G $\lambda$  corresponding to a fringe spacing of  $\sim 140$ – $370$   $\mu$ as. For a fringe spacing much larger than the source size, the visibility amplitude is well approximated by a quadratic function solely governed by the size along the baseline direction and the compact total flux density of the source (Issaoun et al. 2019a). Along with the direction of the SMT–LMT baseline, the EHT array has the ALMA–LMT baseline with intermediate baseline lengths of 2.6–4.2 G $\lambda$  (see Figure 6). The visibility amplitudes on these baselines are useful to constrain the compact total flux density and source size on VLBI scales along the directions of these baselines together with the intra-site short baselines tracing the total flux density on arcsecond scales (see M87\* Paper IV, Appendix B.1).

Here, we derive constraints on the total compact flux density and the source size in a similar manner to M87\* Paper IV by making use of these baselines. Compared with M87\* data presented in M87\* Paper III, Sgr A\* data are further calibrated using interpolated gain solutions from calibrators §5.1.3. We therefore modify the equations in M87\* Paper IV and derive the three constraints outlined below.

*Constraint 1.* The first constraint is based on the fact that the visibility amplitudes fall approximately quadratically with baseline length on short baselines, (Issaoun et al. 2019a). The intermediate-to-long baselines tend to measure larger correlated flux density than what is expected for a Gaussian source with equivalent quadratic amplitude behavior on short baselines. While localized visibility-domain features such as “nulls” may give lower flux densities than the equivalent Gaussian, the presence of image substructure will tend to increase the average flux density. On short baselines, we can thus express the visibility amplitudes in terms of an equivalent circular Gaussian visibility function,

$$V_G(\mathbf{u}; I_0, \theta) = I_0 e^{-\frac{(\pi\theta|\mathbf{u}|)^2}{4\ln 2}}, \quad (5)$$

where  $I_0$  is the total flux density of the Gaussian source,  $|\mathbf{u}|$  is the length of the baseline, and  $\theta$  is its FWHM in radians. We can deduce that the measured amplitude ratio of the ALMA–LMT over SMT–LMT baselines will be larger than the corresponding ratio from a circular Gaussian source model. Consequently, the FWHM size of a circular Gaussian determined by the amplitude ratio between SMT–LMT and ALMA–LMT baselines provides an estimate of the minimum compact source size  $\theta_{\text{cpt}}$  that is not significantly affected by the intrinsic fine-

scale source structure:

$$\theta_{\text{cpt}} \gtrsim \sqrt{\frac{4 \ln 2 \ln \left( \frac{|\mathcal{V}_{\text{SMT-LMT}}|}{|\mathcal{V}_{\text{ALMA-LMT}}|} \right)}{\pi^2 (|\mathbf{u}|_{\text{ALMA-LMT}}^2 - |\mathbf{u}|_{\text{SMT-LMT}}^2)}}. \quad (6)$$

Here,  $\mathcal{V}_{i-j}$  denotes the true visibility on the baseline  $i-j$ . The ratio of the true visibility amplitudes is lower-bounded by

$$\frac{|\mathcal{V}_{\text{SMT-LMT}}|}{|\mathcal{V}_{\text{ALMA-LMT}}|} \geq \left( 1 - \sqrt{\Delta g_{\text{ALMA}}^2 + \Delta g_{\text{SMT}}^2} \right) \frac{|V_{\text{SMT-LMT}}|}{|V_{\text{ALMA-LMT}}|}, \quad (7)$$

where  $V_{i-j}$  and  $\Delta g_i$  denote the calibrated measured visibility and the deviation of its residual station gain from unity, respectively, after gain calibration using calibrators.  $\Delta g_{\text{ALMA}}$  and  $\Delta g_{\text{SMT}}$  are estimated to be 0.05 and 0.06 respectively, corresponding to the standard deviation of gain solutions from calibrator data across multiple imaging methods described in §5.1.3. We take the median of the visibility amplitude ratio from the collection of constraints derived for each single VLBI scan to derive a robust estimate of the minimum source size. With this method, we are able to derive a conservative constraint, which is agnostic to the assumed source structure (e.g., the presence of a null from a ring-like structure).

*Constraint 2.* The second constraint comes from the curvature of visibility amplitudes between the intra-site baselines and the LMT–SMT baseline. Since the compact flux density should not exceed the total flux density measured with the intra-site baselines, the amplitude fall from the intra-site to LMT–SMT baselines gives the maximum limit of that from the compact flux density to LMT–SMT baseline. Therefore, it gives the maximum limit of the source FWHM size with an equivalent circular Gaussian as

$$\theta_{\text{cpt}} \leq \frac{2\sqrt{\ln 2}}{\pi|\mathbf{u}|} \sqrt{\ln \frac{F_{\text{tot}}}{|\mathcal{V}_{\text{LMT-SMT}}|}}. \quad (8)$$

With the residual gain uncertainty, this maximum limit is upper-bounded by

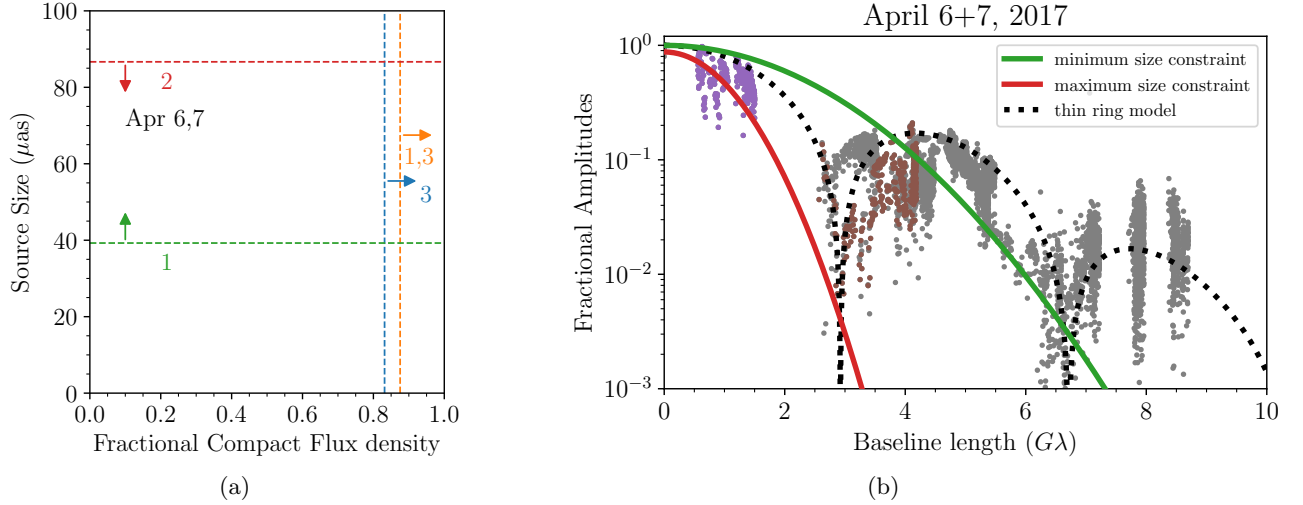
$$\frac{1}{|\mathcal{V}_{\text{LMT-SMT}}|} \leq \frac{1 + \sqrt{\Delta g_{\text{LMT}}^2 + \Delta g_{\text{SMT}}^2 + \Delta g_{\text{tot}}^2}}{|\mathcal{V}_{\text{LMT-SMT}}|}. \quad (9)$$

In the same manner as with other stations,  $\Delta g_{\text{LMT}}$  is estimated to be 0.12 post calibrator gain-transfer.  $\Delta g_{\text{tot}}$ , the fractional uncertainty in the light curve, is estimated to be at most 0.2 based on the consistency of light curves obtained with different instruments / reduction pipelines (see Wielgus et al. 2022). Similarly to Constraint 1, the median of the ratio is adopted to mitigate the effects of statistical errors.

*Constraint 3.* The minimum compact flux density can be derived by the maximum amplitudes of LMT–SMT

**Table 6.** Constraints on fractional compact flux density and source size measured along the directions of the LMT–SMT and LMT–ALMA baselines.

UTC day (2017 April)	Fractional Compact Flux Density	Fractional Compact Flux Density (with the minimum source size)	Minimum Source Size ( $\mu\text{as}$ )	Maximum Source Size ( $\mu\text{as}$ )
6	0.83	0.88	42	79
7	0.66	0.73	38	95
6 + 7	0.83	0.88	39	87

**Figure 11.** Joint constraints on the size and total compact flux density of the 1.3 mm emission in Sgr A\* shown in Table 6. See §5.1.5 for details. (a) Numbered constraints correspond to: (1) the LMT–SMT/LMT–ALMA amplitude ratio, (2) LMT–SMT amplitudes coupled with the requirement  $F_{\text{cpt}} \leq F_{\text{tot}}$ , and (3) the maximum LMT–SMT amplitude. The position angles of the LMT–SMT and LMT–ALMA baselines range from  $125^\circ$  to  $164^\circ$ . (b) Fractional visibility amplitudes of circular Gaussian sources with FWHMs corresponding to the minimum (green line) and maximum (red line) size constraints for the April 6 and 7 data sets. Flux-normalized calibrated amplitudes are overlaid, where those of the LMT–SMT and ALMA–LMT baselines used to derive these size constraints are colored in purple and brown, respectively. The dotted line denotes the thin-ring model shown in Figure 7 for comparison.

baseline, since the visibility amplitudes are maximum at zero baseline length, as given by

$$F_{\text{cpt}} \geq |\mathcal{V}_{\text{SMT-LMT}}| \quad (10)$$

$$\geq (1 - \sqrt{\Delta g_{\text{LMT}}^2 + \Delta g_{\text{SMT}}^2}) |\mathcal{V}_{\text{LMT-SMT}}|. \quad (11)$$

In the above equation, the equality is satisfied in the extreme situation when the source is completely unresolved at the LMT–SMT baseline, whereas in reality it partially resolves the source structure. A stronger constraint is given by the equivalent circular Gaussian with the minimum source size (Constraint 1) extrapolated from the LMT–SMT baselines, described by,

$$F_{\text{cpt}} \geq |\mathcal{V}_{\text{LMT-SMT}}| e^{\frac{(\pi|u|\theta_{\text{cpt}})^2}{4 \ln 2}}. \quad (12)$$

We note that the upper and lower limits on the source size obtained from Constraints 1 and 2 are along the di-

rections of LMT–SMT and LMT–ALMA baselines. Using synthetic data from general relativistic magneto-hydrodynamics (GRMHD) and semi-analytic geometric models in Paper III, we have verified that these size constraints remain valid for various morphologies sharing similar profiles of visibility amplitudes with EHT Sgr A\* data (see Paper III for details).

The derived constraints are summarized in Table 6 and Figure 11 (a) for each observing day and for both days combined. As shown in Figure 11 (b), the equivalent Gaussians with the minimum and maximum sizes reasonably give the upper and lower bounds of the visibility amplitudes, respectively, on short baselines. Either of the source size constraints indicate that the 2017 EHT Sgr A\* data resolve compact emission of several tens of microarcseconds, consistent with the early EHT observations (Doeleman et al. 2008; Fish et al. 2011; Johnson et al. 2015; Lu et al. 2018; Johnson et al. 2018a).



The estimated minimum fractional compact flux density is  $\sim 70 - 90\%$ , indicating that the vast majority of the radio emission from Sgr A\* arises from the horizon-scale emission resolved with the EHT. The maximum limit on the extended emission resolved out on the shortest VLBI baselines is indeed much less than for M87\*, 3C 279, and Centaurus A—all of which are known to have a prominent extended jet (M87\* Paper IV; Kim et al. 2020; Janssen et al. 2021)—as expected by the non-detection of an extended jet in longer-wavelength VLBI observations across many decades (see §5.1.4 and references therein) and early EHT observations.

### 5.1.6. Source variability

Studies of the variability of Sgr A\* light curves at 230 GHz in 2005–2017 (e.g., Marrone et al. 2008; Dexter et al. 2014; Bower et al. 2018) indicate that on long timescales (from a few days to years) the source fluctuates between 2.0 and 4.5 Jy. During the 2017 EHT observations Sgr A\* was in a low luminosity state with a mean flux density of  $\sim 2.4 \pm 0.2$  Jy between 213–229 GHz (Table 2). The two days for which VLBI data analysis is presented in this series of papers exhibit a low degree of variability that is typical for this source, characterized by the modulation index (standard deviation divided by mean)  $\sigma/\mu < 10\%$ . The power spectral density has a red noise character on timescales from 1 min to several hours, with a transition to white noise for longer timescales. On 2017 April 11 the millimeter flux rises by over 50%, following the X-ray flare maximum with a delay of  $\sim 2$  h. The data on this day appear significantly more variable. An analysis of the 2017 April 11 VLBI data will be presented in a separate future publication. A detailed analysis of the full data set of Sgr A\* light curves contemporaneous with the EHT 2017 observations is presented in the companion paper Wielgus et al. (2022).

The  $Q$ -metric (Roelofs et al. 2017) quantifies the variability of a compact source resolved on VLBI baselines in a series of closure phases as a function of time on a specific baseline triangle. The metric compares the observed closure phase variations ( $\hat{\sigma}^2$ ) to those expected from thermal noise ( $\tilde{\epsilon}^2$ ), after detrending the data to account for slow variations due to the evolution of baselines as the Earth rotates (see Roelofs et al. 2017, for details):

$$Q = \frac{\hat{\sigma}^2 - \tilde{\epsilon}^2}{\hat{\sigma}^2}. \quad (13)$$

A static source is expected to give a  $Q$ -metric value close to zero, and a variable source can give a  $Q$ -metric value up to one.

Figure 12 shows the  $Q$ -metric for M87\* and Sgr A\* data after dividing the closure phases into two-hour segments and detrending those with a third-order polynomial. The  $Q$ -metric is generally higher for Sgr A\* than for M87\*, which does not necessarily indicate that

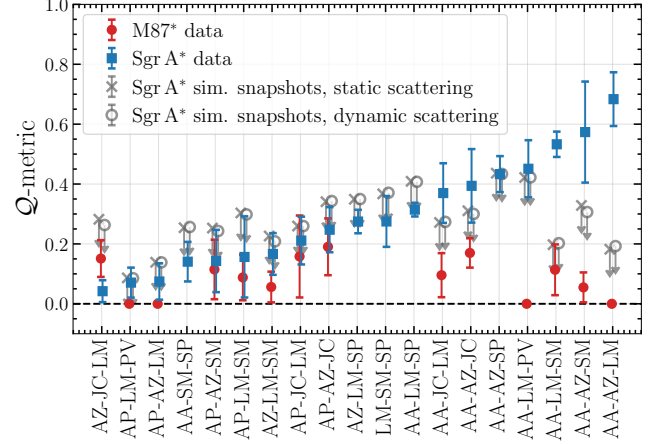


**Figure 12.**  $Q$ -metric values (Equation 13) indicating intrinsic closure phase variability on baseline triangles with mutual visibility of both M87\* and Sgr A\* in ascending order of the Sgr A\* variability. The two-letter station codes are taken from Table 5. Only closure phase tracks with more than ten data points after averaging down to 120 s were used. The closure phase tracks were detrended within two hour segments by subtracting a third-degree polynomial before computing the  $Q$ -metric. The plotted values are averages across days (2017 April 5, 6, 10, and 11 for M87\*, 2017 April 6 and 7 for Sgr A\*) and bands, with the error bars indicating the  $1\sigma$  spread across the days and bands. The  $Q$ -metric for the M87\* and Sgr A\* data are shown in red and blue, respectively. The grey points show  $1\sigma$  upper limits of the distributions of  $Q$ -metric values obtained from synthetic data generated from intrinsically static source models, with either a static or moving scattering screen with parameters from Johnson et al. (2018a), but with an enlarged power-law index of  $\alpha = 1.5$  for the interstellar turbulence to obtain more conservative upper limits of scattering-induced variability. The static source models are a mix of models from the GRMHD library, which contains a large range of source structures, and the models used to calibrate the imaging methods in Paper III. Upper limits are computed based on the maximum  $Q$ -metric values from independent realizations of possible source models and thermal noise on each triangle.

Sgr A\* varies more strongly because of the different error budgets for the two sources. However, the different  $Q$ -metric values do indicate that intrinsic variability is detected with higher significance for Sgr A\* than for M87\*. The measured variability occurs on timescales between the visibility averaging time of 120 s and the two hour long detrending segments. The high sensitivity to thermal noise can lead to different  $Q$ -values on redundant triangles.

Because of imperfections in the detrending procedure (a third-order polynomial does not generally capture any static source structure) and the particular realization of the thermal noise, a static source may also give nonzero

$Q$ -metric values. In order to determine on which triangles we detect significant variability, the measured  $Q$ -metric values are therefore compared to those simulated for a range of static source models for Sgr A\*. Shown in Figure 12 are  $1\sigma$  upper limits of the distributions of  $Q$ -metric values obtained from synthetic data generated from different single static GRMHD-GRRT snapshots (Paper V), with different realizations of either a static or moving scattering screen. We have applied random position angle rotations to 12 random frames drawn from MAD/SANE models with spins of  $\pm 0.94, \pm 0.5, 0$ ,  $R_{\text{high}} = 10, 40$  and inclination angles of  $10^\circ, 30^\circ, 50^\circ, 70^\circ$  (a description of these models and their parameters is given in Paper V). For these 960 different source structures, we have generated synthetic data using 100 different thermal noise realizations for each observing day and the low and high frequency bands. We applied the same procedure to eleven frames of each of the source models used to calibrate the imaging methods in Paper III, which were chosen to match the measured visibility amplitudes of Sgr A\*. The resulting  $Q$ -metric values were bootstrapped to obtain the same number of values as those from the GRMHD models.

Scattering-screen variability generally has a small effect on the  $Q$ -metric. Comparing the measured and simulated  $Q$ -metric values, we see a significant excess for Sgr A\* on ALMA-LMT-SMA, ALMA-SMT-SMA, and ALMA-SMT-LMT. For these triangles, the observed closure phase variability cannot be explained by variability due to interstellar scattering or imperfections in the detrending procedure. The excess variability in degrees  $\dot{Q} = \sqrt{\sigma^2 - \bar{\epsilon}^2}$  is  $16.4^\circ, 6.8^\circ$ , and  $3.1^\circ$  for these triangles, respectively. Hence, although the  $Q$ -metric does indicate intraday closure phase variability in the Sgr A\* data, it only does so on a few triangles, and the variability amplitude is small.

More detailed discussions of the source variability based on static and time-dependent reconstructions of the underlying Sgr A\* source model, as well as examples of typical closure phase trends, are given in Paper III; Paper IV.

## 5.2. Multi-wavelength Data Products

### 5.2.1. mm, NIR, and X-ray data products

The supplementary ground- and space-based data products leveraged here are published in original works and/or are available in public archives.

EAVN observations of Sgr A\* at 22 and 43 GHz are available in Cho et al. (2022), GMVA 86 GHz observations are published in Issaoun et al. (2019b), and a detailed discussion of the VLT/GRAVITY NIR flux distribution can be found in Gravity Collaboration et al. (2020).

Chandra, Swift, and NuSTAR data products are available via NASA archives<sup>14,15,16</sup> and are collected in the EHT data portal<sup>17</sup> under the 2021-DXX-XX code. The repository contains the following data products:

1. Description of observations and data processing (format: text).
2. Fluxes from Swift-XRT observations (format: CSV).
3. Fluxes from Chandra observations (format: CSV).
4. Fluxes from NuSTAR observations (format: CSV).
5. Scripts, spectral, and response files for modeling Chandra and NuSTAR data (format: standard X-ray data formats).
6. Sampled posterior distributions of X-ray spectral model based on Chandra and NuSTAR data (format: FITS).

The EHT data portal also contains the broadband spectrum table (see §5.2.2 below) with frequency, flux density, its uncertainty, and instrument index (format: CSV).

### 5.2.2. Time-averaged spectral energy distribution

Figure 13 displays the SED for Sgr A\* during the 2017 EHT campaign (open black circles) over-plotted on the historically observed broadband spectrum (colored points). The SED illustrates Sgr A\*'s wide range of variable and non-variable states. Larger shaded swaths mark regions of the SED where the source is particularly variable; their bounds mark characteristic quiescent emission and high flux states, which can last for timescales of minutes to hours. (A time-binned historic SED representative of states without extreme variability is presented in Paper VI.) We do not plot a typical quiescent value for NuSTAR frequencies (3–79 keV) since upper-limits are complicated by contributions from non-Sgr A\* sources in the galactic center. The flux and luminosity values from each observatory coordinating during the EHT campaign are listed in Table 2. The quiescent and flare X-ray luminosities in the SED are  $\nu L_\nu$  in units of  $\text{erg s}^{-1}$ ; their equivalent  $\nu F_\nu$  values in  $\text{erg s}^{-1} \text{cm}^{-2}$  (Table 2) differ slightly from the integrated flux values in Table 3.

During the EHT run, Sgr A\*'s SED is consistent with historical observations of the black hole in the radio,

<sup>14</sup> The Chandra Data Archive: <https://cxc.harvard.edu/cda/>.

<sup>15</sup> The Swift Data Archive: <https://swift.gsfc.nasa.gov/archive/>.

<sup>16</sup> The NuSTAR Data Archive: [https://heasarc.gsfc.nasa.gov/docs/nustar/nustar\\_archive.html](https://heasarc.gsfc.nasa.gov/docs/nustar/nustar_archive.html).

<sup>17</sup> <https://eventhorizontelescope.org/for-astronomers/data>

mm, NIR, and X-ray, as outlined in the Introduction and §5.2.3. For example, the moderately bright X-ray flare detected with Chandra and NuSTAR on 2017 April 11 falls within the range of previously observed X-ray flares (see §4.2 and Figure 13). Since Sgr A\* is not in an exceptional state during the 2017 EHT campaign, these observational constraints on the broadband SED offer valuable priors on theoretical models aiming to constrain GR, for example the Kerr metric investigation presented in Paper VI.

Paper V in this series also uses these (quasi-)simultaneous EHT 1.3 mm and multi-wavelength constraints (on both luminosity and degree of variability) to aid in model selection and to provide a physical interpretation for these data, for example by testing aligned, tilted, and stellar wind-fed scenarios using time-dependent GRMHD models. They compare specifically to three MWL bands, 86 GHz,  $2.2\ \mu\text{as}$ , and X-ray, which are relatively independent and thus probe different physics, and find that no one existing model can meet all of the EHT and MWL constraints. These challenges motivate improvements to the GRMHD model suites, and encourage additional, joint EHT and MWL campaigns to fully characterize Sgr A\*'s short and long term variability.

### 5.2.3. Characteristic multi-wavelength variability

Sgr A\*'s multi-wavelength variability has been studied in detail for more than two decades. Substantial obscuration in the plane of the Galaxy blocks our view of its optical and UV emission, but observations at other wavelengths show flickering, flares, and other stochastic processes on long and short timescales (e.g., Baganoff et al. 2001; Dodds-Eden et al. 2009b; Nowak et al. 2012b; Witzel et al. 2012; Neilsen et al. 2015; Bower et al. 2015; Haggard et al. 2019; Do et al. 2019; Gravity Collaboration et al. 2020). Theoretical models also anticipate that observations at different wavelengths will probe different size scales and resolutions (e.g., Falcke & Markoff 2013). We briefly describe Sgr A\*'s characteristic MWL variability, to put the X-ray flares (§4.2.4) and the broadband spectrum (§5.2.2) observed in 2017 into this broader context.

Sgr A\*'s X-ray flux distribution can be decomposed into a steady quiescent component described by a Poisson process, and a variable power law component attributed to non-thermal flares that appear approximately once per day (Neilsen et al. 2015). Sgr A\*'s quiescent NIR light curves show a red noise process and a non-linear, non-Gaussian flux density distribution, skewed to higher flux densities, which changes slope near a median flux density of  $1.1 \pm 0.3$  mJy (flux densities below 0.1 mJy are rarely observed; e.g., Witzel et al. 2012; Do et al. 2019; Gravity Collaboration et al. 2020). Thus the NIR flux can also be attributed to separate quiescent and variable components.

The X-ray and NIR variability timescales are both typically several hours, consistent with Sgr A\*'s ISCO period of approximately 4–30 min for prograde orbits (vs. 5 days to 1 month for M87\*; for further discussion of this comparison, see Paper I). Recently, the orbital motion of a compact polarized hot spot just outside of the ISCO has been offered as an explanation for high resolution, time resolved interferometric NIR observations (Gravity Collaboration et al. 2018), reinforcing the notion that this may be a horizon-scale phenomena.

Correlations between the X-ray and NIR flux peaks (e.g., Dodds-Eden et al. 2009b; Ponti et al. 2017; Boyce et al. 2019; GRAVITY Collaboration et al. 2021; Michail et al. 2021; Boyce et al. 2022) and similarities in their statistical properties and flux density distributions (Witzel et al. 2012, 2018b, 2021; Neilsen et al. 2015) point to a physical connection between the emission at these wavelengths, though the X-ray structure function seems to have less power at short timescales than the NIR structure function (Witzel et al. 2012, 2018a; Neilsen et al. 2015; Witzel et al. 2021).

At submillimeter and radio wavelengths Sgr A\* also shows a quiescent state superposed with almost continuous variability (e.g., Miyazaki et al. 2004; Macquart & Bower 2006; Yusef-Zadeh et al. 2011; Brinkerink et al. 2015). These longer-duration flares may be delayed by a few hours relative to the X-ray/NIR flares, but simultaneous observations are sparse and the correlations remain tenuous (Capellupo et al. 2017). Some submm flares have also been associated with NIR flares, while others show no correlation (Marrone et al. 2008; Morris et al. 2012; Fazio et al. 2018; Michail et al. 2021; Boyce et al. 2022). Iwata et al. (2020) pursued a detailed study of Sgr A\*'s flux density distribution at 217.5, 219.5, and 234.0 GHz, finding variability on timescales of  $\sim 10$ 's of minutes to hours that is likely to arise near the ISCO. They find no lag between 217.5 and 234.0 GHz.

Analysis by Wielgus et al. (2022) based on the ALMA and SMA data associated with this 2017 EHT campaign show Sgr A\* mostly in a quiescent state at 213, 220, and 229 GHz (Figs. 4 and 13), though the 2017 April 11 observations following the X-ray flare show enhanced millimeter wavelength variability. The mm light curves are consistent with a red noise process with the power spectral density slope between  $-2$  and  $-3$  on timescales between 1 minute and several hours. In an independent study, Bower et al. (2018) detect both linear and circular polarization in Sgr A\*'s millimeter emission. They find a mean rotation measure (RM) of  $\sim -5 \times 10^5$  rad m $^{-2}$  and variability on timescales of hours to months. Long-term variability in the RM (of order weeks to months) is likely due to turbulence in the accretion flow, while short-term variability seems to arise from complex emission and propagation effects near the black hole. They also detect circular polarization with a mean value of  $-1.1 \pm 0.2\%$  that is variable on timescales of hours to months (Bower et al. 2018). EHT polarimetric measure-

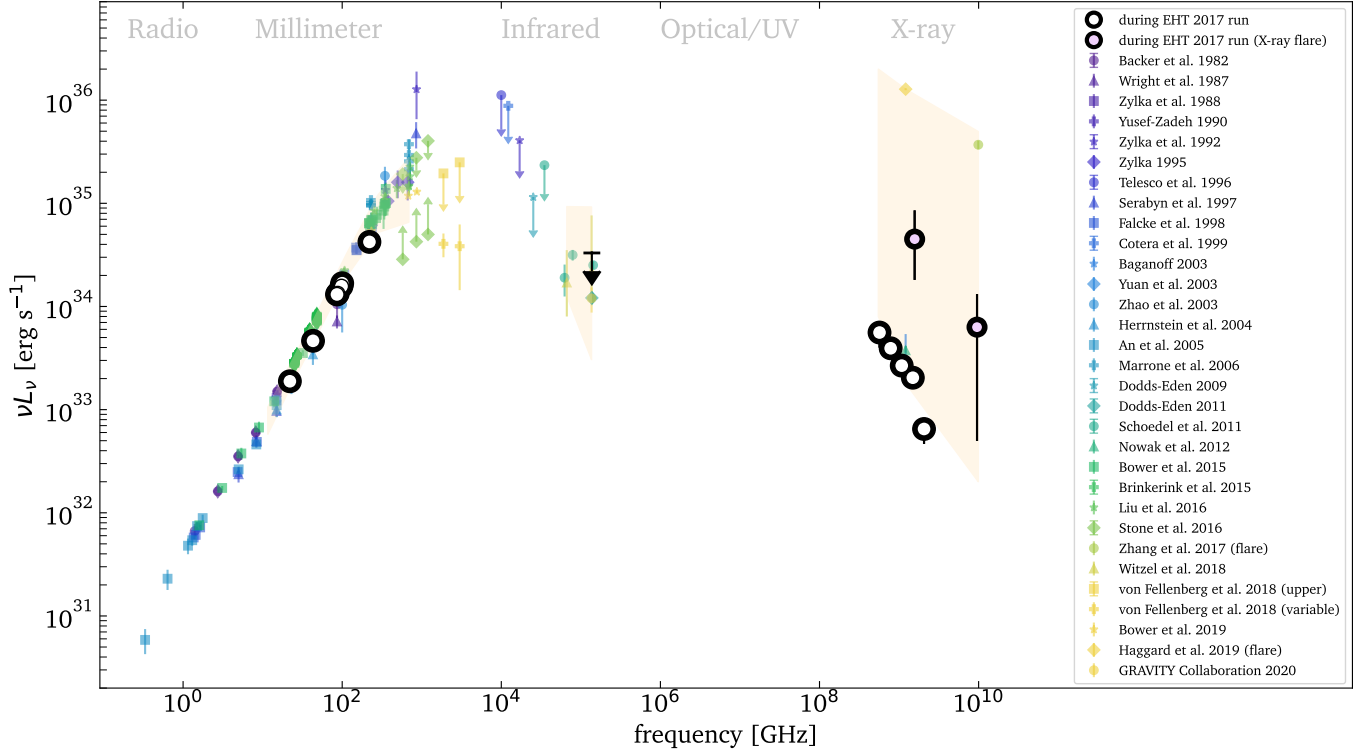


**Figure 13.** The time-averaged SED for the compact Sgr A\* source during the 2017 EHT run is shown as black open circles and a NIR upper limit. Luminosities for the X-ray flare observed on 2017 April 11 are indicated as black circles filled with light purple. Table 2 lists the 2017 values in units of flux and luminosity. Colored background points display the historic SED of Sgr A\* in flaring and quiescent states with the light yellow polygons indicating the range of previously observed variability (Backer 1982; Zylka & Mezger 1988; Wright et al. 1987; Yusef-Zadeh et al. 1990; Zylka et al. 1992, 1995; Telesco et al. 1996; Serabyn et al. 1997; Falcke et al. 1998; Cotera et al. 1999; Baganoff et al. 2003b; Yuan et al. 2003; Zhao et al. 2003; Herrnstein et al. 2004; An et al. 2005; Marrone et al. 2006b; Dodds-Eden et al. 2009a, 2011; Schödel et al. 2011; Nowak et al. 2012b; Bower et al. 2015; Brinkerink et al. 2015; Liu et al. 2016; Stone et al. 2016; Zhang et al. 2017b; Witzel et al. 2018a; Haggard et al. 2019; von Fellenberg et al. 2018; Bower et al. 2019; Gravity Collaboration et al. 2020). A time-binned historic SED representative of states without extreme variability is presented in Paper VI.

ments of Sgr A\* will be the subject of future works in this series.

These and other MWL observations have led to broad consensus that near Sgr A\*'s event horizon there are two components: (1) a relatively stable quiescent accretion flow, and (2) flares or bright flux excursions that vary on shorter timescales. Accretion models for Sgr A\* suggest that the system may drive a jet, and some data support this possibility. For example, an observed increase of variability amplitude with frequency and persistent time lags in the 18–43 GHz band may be indicative of a jet outflow (Brinkerink et al. 2021). Yet despite this and other tentative claims at  $\gamma$ -ray, X-ray, and radio wavelengths (e.g., Su & Finkbeiner 2012; Li et al. 2013; Zhu et al. 2019; Yusef-Zadeh et al. 2012; Rauch et al. 2016), a jet has not yet been conclusively confirmed. The accretion flow and the jet base are both candidates to drive Sgr A\*'s variability (e.g., the base of the jet very likely dominates the emission near M87\*), yet while their

timescales may be distinct, the base of a jet and a variable RIAF remain difficult to tell apart (see Paper V).

Interstellar scattering may induce additional variable signals over timescales similar to (or longer than) those from the quiescent accretion flow. For example, one explanation for the detectability of the GC magnetar was a variable scattering screen (Eatough et al. 2013; Bower et al. 2014b). Meanwhile, interactions with orbiting objects may cause additional variability, e.g., disruptions of  $\sim$ km-sized rocky bodies, gaseous structures, or other interlopers (Čadež et al. 2008; Kostić et al. 2009; Zubovas et al. 2012; Gillessen et al. 2012; Cürlo et al. 2020; Peißker et al. 2021). Contemporaneous observations with EHT and MWL facilities, particularly simultaneous capture of serendipitous events like flares, continue to offer the best opportunity for disentangling these contributions to Sgr A\*'s variable emission.

## 6. SUMMARY AND CONCLUSIONS



Sgr A\* and M87\* are the primary targets of the EHT, for which the April 2017 observing campaign provided the required resolution and sensitivity to obtain horizon-scale images of these supermassive black holes. M87\* total intensity and polarization results from the 2017 data have been published earlier (M87\* Paper I; M87\* Paper II; M87\* Paper III; M87\* Paper IV; M87\* Paper V; M87\* Paper VI; M87\* Paper VII; M87\* Paper VIII). In this new series of papers (Paper I; Paper II; Paper III; Paper IV; Paper V; Paper VI), we present the imaging, analysis, and interpretation of the 2017 Sgr A\* EHT and accompanying data at X-ray, NIR, and millimeter wavelengths from EAVN, GMVA, VLT/NACO, Swift, Chandra, and NuSTAR. Sgr A\* was observed by the EHT on 2017 April 5, 6, 7, 10, and 11. In this series of papers, we focus our analysis on the days with the best  $(u, v)$ -coverage, 2017 April 6 and 7; a detailed analysis of the full set of Sgr A\* millimeter light curves can be found in the companion paper by Wielgus et al. (2022).

We use the two independent pipelines EHT-HOPS (Blackburn et al. 2019) and rPICARD (Janssen et al. 2018, 2019b) for the calibration of the EHT data. By utilizing the data from both pipelines, we obtain scientific results in a robust manner, independent of assumptions made for the data calibration. With various jack-knife tests, we estimate the amount of systematic noise present in the EHT data and verify that data issues are mitigated.

We present updates to the a priori gain calibration for several EHT stations. Additionally, we perform a network calibration (Blackburn et al. 2019) based on the total flux of the source to correct the gains of the co-located EHT stations. To account for the rapid flux variability of Sgr A\* in this process, we use light curves obtained at a short intra-scan cadence from the ALMA and SMA connected element interferometers. Finally, we transfer gain solutions from self-calibration solutions of the co-observed J1924–2914 and NRAO 530 calibrator sources. With the time-dependent network calibration and calibrator gains transfer, it is possible to partially correct for time-variable station gain errors that are difficult to solve for using the Sgr A\* data alone due to intrinsic source variability.

The calibrated visibility amplitudes can be described by a blurred ring with a diameter of  $\sim 50 \mu\text{as}$  (a deeper discussion of the source size and morphology can be found in Paper III and Paper IV). The majority of the total flux measured in our VLBI experiment arises from horizon scales in Sgr A\*. Using multi-wavelength constraints on the interstellar scattering screen towards Sgr A\*, we show that the scattering-induced angular broadening of the source is sub-dominant to the intrinsic

source structure uncovered by the EHT. The refractive noise added by the scattering screen is only relevant for data at baseline lengths  $\gtrsim 6 \text{ G}\lambda$ .

Without making strong assumptions about the source structure, we find a compact source size of  $39\text{--}87 \mu\text{as}$  for Sgr A\*, which is in agreement with earlier 1.3 mm VLBI observations of the source. A more precise modeling-based estimation of the source size is given in Paper III. On 2017 April 6 and 7, the source was in a low luminosity state, where the total flux fluctuates around  $2.4 \text{ Jy}$  with a modulation index of less than 10%. The Sgr A\* closure phases show clear intrinsic structural variability on timescales of a few minutes to a few hours that is further investigated in Paper III; Paper IV.

Multi-wavelength observations show that Sgr A\* was in a mostly quiescent state, with broadband flux levels consistent with historical measures. We detect two X-ray flares: one very faint flare on 2017 April 7 and a brighter flare on 2017 April 11. The fainter 2017 April 7 flare is detected at low significance by Swift and Chandra, and the brighter 2017 April 11 flare is detected more confidently by Chandra and NuSTAR. ALMA and SMA 2017 April 11 observations begin immediately after the bright X-ray flare and show enhanced millimeter wavelength variability (Wielgus et al. 2022). These multi-wavelength data offer important constraints for theoretical models; indeed, no one of the GRMHD models presented in Paper V can match the full suite of multi-wavelength constraints. These unprecedented EHT and MWL data thus provide a rich opportunity to improve models of Sgr A\* and to advance our understanding of the physics near the SMBH event horizon. The high quality, nearly simultaneous multi-wavelength SED is additionally valuable for understanding the priors for sophisticated tests of GR (see Paper VI). Looking ahead, future detailed analysis of the EHT and MWL observations on 2017 April 11 holds great promise for understanding the underlying mechanisms that drive Sgr A\*'s flares and other variability.

## ACKNOWLEDGMENTS

*Facilities:* EHT, ALMA, APEX, IRAM:30m, JCMT, LMT, SMA, ARO:SMT, SPT, Chandra, EAVN, GMVA, NuSTAR, Swift, VLT.

*Software:* DiFX (Deller et al. 2011), CALC, PolConvert (Martí-Vidal et al. 2016), HOPS (Whitney et al. 2004), EHT-HOPS Pipeline (Blackburn et al. 2019), CASA (McMullin et al. 2007), rPICARD (Janssen et al. 2018, 2019b)

## REFERENCES

- Alef, W., & Porcas, R. W. 1986, A&A, 168, 365
- An, T., Goss, W. M., Zhao, J.-H., et al. 2005, ApJL, 634, L49, doi: [10.1086/498687](https://doi.org/10.1086/498687)

- An, T., Sohn, B. W., & Imai, H. 2018, *Nature Astronomy*, 2, 118, doi: [10.1038/s41550-017-0277-z](https://doi.org/10.1038/s41550-017-0277-z)
- Backer, D. 1982, in *Extragalactic Radio Sources*, ed. D. S. Heeschen & C. M. Wade, Vol. 97, 389
- Baganoff, F. K., Bautz, M. W., Brandt, W. N., et al. 2001, *Nature*, 413, 45, doi: [10.1038/35092510](https://doi.org/10.1038/35092510)
- Baganoff, F. K., Maeda, Y., Morris, M., et al. 2003a, *ApJ*, 591, 891, doi: [10.1086/375145](https://doi.org/10.1086/375145)
- . 2003b, *ApJ*, 591, 891, doi: [10.1086/375145](https://doi.org/10.1086/375145)
- Bardeen, J. M. 1973, in *Black Holes (Les Astres Occlus)*, 215–239
- Blackburn, L., Pesce, D. W., Johnson, M. D., et al. 2020, *ApJ*, 894, 31, doi: [10.3847/1538-4357/ab8469](https://doi.org/10.3847/1538-4357/ab8469)
- Blackburn, L., Chan, C.-k., Crew, G. B., et al. 2019, *ApJ*, 882, 23, doi: [10.3847/1538-4357/ab328d](https://doi.org/10.3847/1538-4357/ab328d)
- Bower, G. C., Falcke, H., Herrnstein, R. M., et al. 2004a, *Science*, 304, 704, doi: [10.1126/science.1094023](https://doi.org/10.1126/science.1094023)
- . 2004b, *Science*, 304, 704, doi: [10.1126/science.1094023](https://doi.org/10.1126/science.1094023)
- Bower, G. C., Goss, W. M., Falcke, H., Backer, D. C., & Lithwick, Y. 2006, *ApJL*, 648, L127, doi: [10.1086/508019](https://doi.org/10.1086/508019)
- Bower, G. C., Deller, A., Demorest, P., et al. 2014a, *ApJL*, 780, L2, doi: [10.1088/2041-8205/780/1/L2](https://doi.org/10.1088/2041-8205/780/1/L2)
- . 2014b, *ApJL*, 780, L2, doi: [10.1088/2041-8205/780/1/L2](https://doi.org/10.1088/2041-8205/780/1/L2)
- Bower, G. C., Markoff, S., Dexter, J., et al. 2015, *ApJ*, 802, 69, doi: [10.1088/0004-637X/802/1/69](https://doi.org/10.1088/0004-637X/802/1/69)
- Bower, G. C., Broderick, A., Dexter, J., et al. 2018, *ApJ*, 868, 101, doi: [10.3847/1538-4357/aae983](https://doi.org/10.3847/1538-4357/aae983)
- Bower, G. C., Dexter, J., Asada, K., et al. 2019, *ApJL*, 881, L2, doi: [10.3847/2041-8213/ab3397](https://doi.org/10.3847/2041-8213/ab3397)
- Boyce, H., A, A., B, B., & C, C. 2022, *ApJ* submitted, 00, 0, doi: TBD
- Boyce, H., Haggard, D., Witzel, G., et al. 2019, *ApJ*, 871, 161, doi: [10.3847/1538-4357/aaf71f](https://doi.org/10.3847/1538-4357/aaf71f)
- Brinkerink, C., Falcke, H., Brunthaler, A., & Law, C. 2021, *arXiv e-prints*, arXiv:2107.13402, <https://arxiv.org/abs/2107.13402>
- Brinkerink, C. D., Falcke, H., Law, C. J., et al. 2015, *A&A*, 576, A41, doi: [10.1051/0004-6361/201424783](https://doi.org/10.1051/0004-6361/201424783)
- Broderick, A. E., & Pesce, D. W. 2020, *ApJ*, 904, 126, doi: [10.3847/1538-4357/abbd9d](https://doi.org/10.3847/1538-4357/abbd9d)
- Burrows, D. N., Hill, J. E., Nousek, J. A., et al. 2005, *SSRv*, 120, 165, doi: [10.1007/s11214-005-5097-2](https://doi.org/10.1007/s11214-005-5097-2)
- Butler, B. 2012, *ALMA Memo Series*, 594
- Capellupo, D. M., Haggard, D., Choux, N., et al. 2017, *ApJ*, 845, 35, doi: [10.3847/1538-4357/aa7da6](https://doi.org/10.3847/1538-4357/aa7da6)
- Cash, W. 1979, *ApJ*, 228, 939, doi: [10.1086/156922](https://doi.org/10.1086/156922)
- Cho, I., Zhao, G.-Y., Kawashima, T., et al. 2022, *ApJ*, 926, 108, doi: [10.3847/1538-4357/ac4165](https://doi.org/10.3847/1538-4357/ac4165)
- Ciurlo, A., Campbell, R. D., Morris, M. R., et al. 2020, *Nature*, 577, 337, doi: [10.1038/s41586-019-1883-y](https://doi.org/10.1038/s41586-019-1883-y)
- Cotera, A., Morris, M., Ghez, A. M., et al. 1999, in *Astronomical Society of the Pacific Conference Series*, Vol. 186, *The Central Parsecs of the Galaxy*, ed. H. Falcke, A. Cotera, W. J. Duschl, F. Melia, & M. J. Rieke, 240
- Coti Zelati, F., Rea, N., Papitto, A., et al. 2015, *MNRAS*, 449, 2685, doi: [10.1093/mnras/stv480](https://doi.org/10.1093/mnras/stv480)
- Coti Zelati, F., Rea, N., Turolla, R., et al. 2017, *MNRAS*, 471, 1819, doi: [10.1093/mnras/stx1700](https://doi.org/10.1093/mnras/stx1700)
- Cui, Y., Hada, K., Kino, M., et al. 2021, *arXiv e-prints*, arXiv:2104.05525, <https://arxiv.org/abs/2104.05525>
- Davies, R. D., Walsh, D., & Booth, R. S. 1976, *MNRAS*, 177, 319, doi: [10.1093/mnras/177.2.319](https://doi.org/10.1093/mnras/177.2.319)
- Degenaar, N., Miller, J. M., Kennea, J., et al. 2013a, *ApJ*, 769, 155, doi: [10.1088/0004-637X/769/2/155](https://doi.org/10.1088/0004-637X/769/2/155)
- . 2013b, *ApJ*, 769, 155, doi: [10.1088/0004-637X/769/2/155](https://doi.org/10.1088/0004-637X/769/2/155)
- Degenaar, N., Wijnands, R., Miller, J. M., et al. 2015, *Journal of High Energy Astrophysics*, 7, 137, doi: [10.1016/j.jheap.2015.03.005](https://doi.org/10.1016/j.jheap.2015.03.005)
- Deller, A. T., Briskin, W. F., Phillips, C. J., et al. 2011, *PASP*, 123, 275, doi: [10.1086/658907](https://doi.org/10.1086/658907)
- Dexter, J., Kelly, B., Bower, G. C., et al. 2014, *MNRAS*, 442, 2797, doi: [10.1093/mnras/stu1039](https://doi.org/10.1093/mnras/stu1039)
- Dexter, J., Deller, A., Bower, G. C., et al. 2017, *MNRAS*, 471, 3563, doi: [10.1093/mnras/stx1777](https://doi.org/10.1093/mnras/stx1777)
- Do, T., Witzel, G., Gautam, A. K., et al. 2019, *ApJL*, 882, L27, doi: [10.3847/2041-8213/ab38c3](https://doi.org/10.3847/2041-8213/ab38c3)
- Dodds-Eden, K., Porquet, D., Trap, G., et al. 2009a, *ApJ*, 698, 676, doi: [10.1088/0004-637X/698/1/676](https://doi.org/10.1088/0004-637X/698/1/676)
- . 2009b, *ApJ*, 698, 676, doi: [10.1088/0004-637X/698/1/676](https://doi.org/10.1088/0004-637X/698/1/676)
- Dodds-Eden, K., Gillessen, S., Fritz, T. K., et al. 2011, *ApJ*, 728, 37, doi: [10.1088/0004-637X/728/1/37](https://doi.org/10.1088/0004-637X/728/1/37)
- Doeleman, S. S., Weintroub, J., Rogers, A. E. E., et al. 2008, *Nature*, 455, 78, doi: [10.1038/nature07245](https://doi.org/10.1038/nature07245)
- Doi, A., Fujisawa, K., Harada, K., et al. 2006, in *Proceedings of the 8th European VLBI Network Symposium*, 71, <https://arxiv.org/abs/astro-ph/0612528>
- Eatough, R. P., Falcke, H., Karuppusamy, R., et al. 2013, *Nature*, 501, 391, doi: [10.1038/nature12499](https://doi.org/10.1038/nature12499)
- Event Horizon Telescope Collaboration, Akiyama, K., Alberdi, A., et al. 2019a, *ApJL*, 875, L1, doi: [10.3847/2041-8213/ab0ec7](https://doi.org/10.3847/2041-8213/ab0ec7)
- . 2019b, *ApJL*, 875, L2, doi: [10.3847/2041-8213/ab0c96](https://doi.org/10.3847/2041-8213/ab0c96)
- . 2019c, *ApJL*, 875, L3, doi: [10.3847/2041-8213/ab0c57](https://doi.org/10.3847/2041-8213/ab0c57)
- . 2019d, *ApJL*, 875, L4, doi: [10.3847/2041-8213/ab0e85](https://doi.org/10.3847/2041-8213/ab0e85)
- . 2019e, *ApJL*, 875, L5, doi: [10.3847/2041-8213/ab0f43](https://doi.org/10.3847/2041-8213/ab0f43)
- . 2019f, *ApJL*, 875, L6, doi: [10.3847/2041-8213/ab1141](https://doi.org/10.3847/2041-8213/ab1141)
- . 2021a, *ApJL*, 875, 1

- . 2021b, *ApJL*, 875, 2
- . 2021c, *ApJL*, 875, 3
- . 2021d, *ApJL*, 875, 4
- . 2021e, *ApJL*, 875, 5
- . 2021f, *ApJL*, 875, 6
- . 2021g, *ApJL*, 875, L7
- . 2021h, *ApJL*, 875, L8
- Falcke, H., Goss, W. M., Matsuo, H., et al. 1998, *ApJ*, 499, 731, doi: [10.1086/305687](https://doi.org/10.1086/305687)
- Falcke, H., & Markoff, S. B. 2013, *Classical and Quantum Gravity*, 30, 244003, doi: [10.1088/0264-9381/30/24/244003](https://doi.org/10.1088/0264-9381/30/24/244003)
- Falcke, H., Melia, F., & Agol, E. 2000, *ApJL*, 528, L13, doi: [10.1086/312423](https://doi.org/10.1086/312423)
- Fazio, G. G., Hora, J. L., Witzel, G., et al. 2018, *ApJ*, 864, 58, doi: [10.3847/1538-4357/aad4a2](https://doi.org/10.3847/1538-4357/aad4a2)
- Fish, V. L., Doeleman, S. S., Beaudoin, C., et al. 2011, *ApJL*, 727, L36, doi: [10.1088/2041-8205/727/2/L36](https://doi.org/10.1088/2041-8205/727/2/L36)
- Fish, V. L., Johnson, M. D., Doeleman, S. S., et al. 2016, *ApJ*, 820, 90, doi: [10.3847/0004-637X/820/2/90](https://doi.org/10.3847/0004-637X/820/2/90)
- Frail, D. A., Diamond, P. J., Cordes, J. M., & van Langevelde, H. J. 1994, *ApJ*, 427, L43, doi: [10.1086/187360](https://doi.org/10.1086/187360)
- Fruscione, A., McDowell, J. C., Allen, G. E., et al. 2006, in *Society of Photo-Optical Instrumentation Engineers (SPIE) Conference Series*, Vol. 6270, Society of Photo-Optical Instrumentation Engineers (SPIE) Conference Series, ed. D. R. Silva & R. E. Doxsey, 62701V, doi: [10.1117/12.671760](https://doi.org/10.1117/12.671760)
- Gehrels, N., Chincarini, G., Giommi, P., et al. 2004, *ApJ*, 611, 1005, doi: [10.1086/422091](https://doi.org/10.1086/422091)
- Genzel, R., Eisenhauer, F., & Gillessen, S. 2010, *Reviews of Modern Physics*, 82, 3121, doi: [10.1103/RevModPhys.82.3121](https://doi.org/10.1103/RevModPhys.82.3121)
- Genzel, R., Schödel, R., Ott, T., et al. 2003, *Nature*, 425, 934, doi: [10.1038/nature02065](https://doi.org/10.1038/nature02065)
- Ghez, A. M., Wright, S. A., Matthews, K., et al. 2004, *ApJL*, 601, L159, doi: [10.1086/382024](https://doi.org/10.1086/382024)
- Gillessen, S., Genzel, R., Fritz, T. K., et al. 2012, *Nature*, 481, 51, doi: [10.1038/nature10652](https://doi.org/10.1038/nature10652)
- Goddi, C., Martí-Vidal, I., Messias, H., & et al. 2021, *ApJL*, 910, L14, doi: [10.3847/2041-8213/abee6a](https://doi.org/10.3847/2041-8213/abee6a)
- Goddi, C., Martí-Vidal, I., Messias, H., et al. 2019, *PASP*, 131, 075003, doi: [10.1088/1538-3873/ab136a](https://doi.org/10.1088/1538-3873/ab136a)
- Goodman, J., & Narayan, R. 1989, *MNRAS*, 238, 995
- Gravity Collaboration, Abuter, R., Accardo, M., et al. 2017, *A&A*, 602, A94, doi: [10.1051/0004-6361/201730838](https://doi.org/10.1051/0004-6361/201730838)
- Gravity Collaboration, Abuter, R., Amorim, A., et al. 2018, *A&A*, 618, L10, doi: [10.1051/0004-6361/201834294](https://doi.org/10.1051/0004-6361/201834294)
- . 2020, *A&A*, 638, A2, doi: [10.1051/0004-6361/202037717](https://doi.org/10.1051/0004-6361/202037717)
- GRAVITY Collaboration, Abuter, R., Amorim, A., et al. 2021, *A&A*, 654, A22, doi: [10.1051/0004-6361/202140981](https://doi.org/10.1051/0004-6361/202140981)
- Greisen, E. W. 2003, in *Astrophysics and Space Science Library*, Vol. 285, Information Handling in Astronomy - Historical Vistas, ed. A. Heck, 109, doi: [10.1007/0-306-48080-8\\_7](https://doi.org/10.1007/0-306-48080-8_7)
- Greve, A., Torres, M., Wink, J. E., et al. 1995, *A&A*, 299, L33
- Gwinn, C. R., Kovalev, Y. Y., Johnson, M. D., & Soglasnov, V. A. 2014, *ApJL*, 794, L14, doi: [10.1088/2041-8205/794/1/L14](https://doi.org/10.1088/2041-8205/794/1/L14)
- Haggard, D., Nynka, M., Mon, B., et al. 2019, *ApJ*, 886, 96, doi: [10.3847/1538-4357/ab4a7f](https://doi.org/10.3847/1538-4357/ab4a7f)
- Hamaker, J. P., Bregman, J. D., & Sault, R. J. 1996, *A&AS*, 117, 137
- Harrison, F. A., Craig, W. W., Christensen, F. E., et al. 2013, *ApJ*, 770, 103, doi: [10.1088/0004-637X/770/2/103](https://doi.org/10.1088/0004-637X/770/2/103)
- Herrnstein, R. M., Zhao, J.-H., Bower, G. C., & Goss, W. M. 2004, *AJ*, 127, 3399, doi: [10.1086/420711](https://doi.org/10.1086/420711)
- Issaoun, S., Folkers, T. W., Blackburn, L., et al. 2017, A conceptual overview of single-dish absolute amplitude calibration, Tech. rep.
- Issaoun, S., Johnson, M. D., Blackburn, L., et al. 2019a, *A&A*, 629, A32, doi: [10.1051/0004-6361/201936156](https://doi.org/10.1051/0004-6361/201936156)
- . 2019b, *ApJ*, 871, 30, doi: [10.3847/1538-4357/aaf732](https://doi.org/10.3847/1538-4357/aaf732)
- . 2021, *ApJ*, 915, 99, doi: [10.3847/1538-4357/ac00b0](https://doi.org/10.3847/1538-4357/ac00b0)
- Issaoun, S., et al. 2022, in prep.
- Iwata, Y., Oka, T., Tsuboi, M., Miyoshi, M., & Takekawa, S. 2020, *ApJL*, 892, L30, doi: [10.3847/2041-8213/ab800d](https://doi.org/10.3847/2041-8213/ab800d)
- Janssen, M., Blackburn, L., Issaoun, S., et al. 2019a, A priori calibration of EHT stations, Tech. rep.
- Janssen, M., Goddi, C., Falcke, H., et al. 2018, in *14th European VLBI Network Symposium & Users Meeting (EVN 2018)*, 80
- Janssen, M., Goddi, C., van Bemmelen, I. M., et al. 2019b, *A&A*, 626, A75, doi: [10.1051/0004-6361/201935181](https://doi.org/10.1051/0004-6361/201935181)
- Janssen, M., Falcke, H., Kadler, M., et al. 2021, *Nature Astronomy*, 5, 1017, doi: [10.1038/s41550-021-01417-w](https://doi.org/10.1038/s41550-021-01417-w)
- Jauncey, D. L., Tzioumis, A. K., Preston, R. A., et al. 1989, *AJ*, 98, 44, doi: [10.1086/115125](https://doi.org/10.1086/115125)
- Johnson, M. D., & Gwinn, C. R. 2015, *ApJ*, 805, 180, doi: [10.1088/0004-637X/805/2/180](https://doi.org/10.1088/0004-637X/805/2/180)
- Johnson, M. D., & Narayan, R. 2016, *ApJ*, 826, 170, doi: [10.3847/0004-637X/826/2/170](https://doi.org/10.3847/0004-637X/826/2/170)
- Johnson, M. D., Fish, V. L., Doeleman, S. S., et al. 2015, *Science*, 350, 1242, doi: [10.1126/science.aac7087](https://doi.org/10.1126/science.aac7087)
- Johnson, M. D., Narayan, R., Psaltis, D., et al. 2018a, *ApJ*, 865, 104, doi: [10.3847/1538-4357/aadcff](https://doi.org/10.3847/1538-4357/aadcff)
- . 2018b, *ApJ*, 865, 104. <https://arxiv.org/abs/1808.08966>
- Jorstad, S., et al. 2022, in prep.

- Kim, J.-Y., Krichbaum, T. P., Broderick, A. E., et al. 2020, *A&A*, 640, A69, doi: [10.1051/0004-6361/202037493](https://doi.org/10.1051/0004-6361/202037493)
- Kostić, U., Čadež, A., Calvani, M., & Gomboc, A. 2009, *A&A*, 496, 307, doi: [10.1051/0004-6361/200811059](https://doi.org/10.1051/0004-6361/200811059)
- Krichbaum, T. P., Graham, D. A., Greve, A., et al. 1997, *A&A*, 323, L17
- Krichbaum, T. P., Graham, D. A., Witzel, A., et al. 1998, *A&A*, 335, L106
- Lee, S.-S., Petrov, L., Byun, D.-Y., et al. 2014, *AJ*, 147, 77, doi: [10.1088/0004-6256/147/4/77](https://doi.org/10.1088/0004-6256/147/4/77)
- Li, Z., Morris, M. R., & Baganoff, F. K. 2013, *ApJ*, 779, 154, doi: [10.1088/0004-637X/779/2/154](https://doi.org/10.1088/0004-637X/779/2/154)
- Liu, H. B., Wright, M. C. H., Zhao, J.-H., et al. 2016, *A&A*, 593, A107, doi: [10.1051/0004-6361/201628731](https://doi.org/10.1051/0004-6361/201628731)
- Liu, S., Petrosian, V., & Melia, F. 2004, *ApJL*, 611, L101, doi: [10.1086/423985](https://doi.org/10.1086/423985)
- Lo, K. Y., & Claussen, M. J. 1983, *Nature*, 306, 647, doi: [10.1038/306647a0](https://doi.org/10.1038/306647a0)
- Lo, K. Y., Shen, Z.-Q., Zhao, J.-H., & Ho, P. T. P. 1998, *ApJL*, 508, L61, doi: [10.1086/311726](https://doi.org/10.1086/311726)
- Lu, R.-S., Krichbaum, T. P., Roy, A. L., et al. 2018, *ApJ*, 859, 60, doi: [10.3847/1538-4357/aabe2e](https://doi.org/10.3847/1538-4357/aabe2e)
- Macquart, J.-P., & Bower, G. C. 2006, *ApJ*, 641, 302, doi: [10.1086/500317](https://doi.org/10.1086/500317)
- Marrone, D. P., Moran, J. M., Zhao, J.-H., & Rao, R. 2006a, *ApJ*, 640, 308, doi: [10.1086/500106](https://doi.org/10.1086/500106)
- Marrone, D. P., Moran, J. M., Zhao, J.-H., & Rao, R. 2006b, in *Journal of Physics Conference Series*, Vol. 54, *Journal of Physics Conference Series*, 354–362, doi: [10.1088/1742-6596/54/1/056](https://doi.org/10.1088/1742-6596/54/1/056)
- . 2007, *ApJL*, 654, L57, doi: [10.1086/510850](https://doi.org/10.1086/510850)
- Marrone, D. P., Baganoff, F. K., Morris, M. R., et al. 2008, *ApJ*, 682, 373, doi: [10.1086/588806](https://doi.org/10.1086/588806)
- Martí-Vidal, I., Roy, A., Conway, J., & Zensus, A. J. 2016, *A&A*, 587, A143, doi: [10.1051/0004-6361/201526063](https://doi.org/10.1051/0004-6361/201526063)
- Matthews, L. D., Crew, G. B., Doeleman, S. S., et al. 2018, *PASP*, 130, 015002, doi: [10.1088/1538-3873/aa9c3d](https://doi.org/10.1088/1538-3873/aa9c3d)
- McMullin, J. P., Waters, B., Schiebel, D., Young, W., & Golap, K. 2007, in *Astronomical Society of the Pacific Conference Series*, Vol. 376, *Astronomical Data Analysis Software and Systems XVI*, ed. R. A. Shaw, F. Hill, & D. J. Bell, 127
- Michail, J. M., Wardle, M., Yusef-Zadeh, F., & Kunneriath, D. 2021, *ApJ*, 923, 54, doi: [10.3847/1538-4357/ac2d2c](https://doi.org/10.3847/1538-4357/ac2d2c)
- Miyazaki, A., Tsutsumi, T., & Tsuboi, M. 2004, *ApJL*, 611, L97, doi: [10.1086/424004](https://doi.org/10.1086/424004)
- Mori, K., Gotthelf, E. V., Zhang, S., et al. 2013, *ApJL*, 770, L23, doi: [10.1088/2041-8205/770/2/L23](https://doi.org/10.1088/2041-8205/770/2/L23)
- Morris, M. R., Meyer, L., & Ghez, A. M. 2012, *Research in Astronomy and Astrophysics*, 12, 995, doi: [10.1088/1674-4527/12/8/007](https://doi.org/10.1088/1674-4527/12/8/007)
- Narayan, R. 1992, *Royal Society of London Philosophical Transactions Series A*, 341, 151, doi: [10.1098/rsta.1992.0090](https://doi.org/10.1098/rsta.1992.0090)
- Neilsen, J., Nowak, M. A., Gammie, C., et al. 2013a, *ApJ*, 774, 42, doi: [10.1088/0004-637X/774/1/42](https://doi.org/10.1088/0004-637X/774/1/42)
- . 2013b, *ApJ*, 774, 42, doi: [10.1088/0004-637X/774/1/42](https://doi.org/10.1088/0004-637X/774/1/42)
- . 2013c, *ApJ*, 774, 42, doi: [10.1088/0004-637X/774/1/42](https://doi.org/10.1088/0004-637X/774/1/42)
- Neilsen, J., Markoff, S., Nowak, M. A., et al. 2015, *ApJ*, 799, 199, doi: [10.1088/0004-637X/799/2/199](https://doi.org/10.1088/0004-637X/799/2/199)
- Niinuma, K., Lee, S.-S., Kino, M., & Sohn, B. W. 2015, *Publication of Korean Astronomical Society*, 30, 637, doi: [10.5303/PKAS.2015.30.2.637](https://doi.org/10.5303/PKAS.2015.30.2.637)
- Nowak, M. A., Neilsen, J., Markoff, S. B., et al. 2012a, *ApJ*, 759, 95, doi: [10.1088/0004-637X/759/2/95](https://doi.org/10.1088/0004-637X/759/2/95)
- . 2012b, *ApJ*, 759, 95, doi: [10.1088/0004-637X/759/2/95](https://doi.org/10.1088/0004-637X/759/2/95)
- Padin, S., Woody, D. P., Hodges, M. W., et al. 1990, *ApJL*, 360, L11, doi: [10.1086/185800](https://doi.org/10.1086/185800)
- Peißker, F., Zajaček, M., Eckart, A., et al. 2021, *ApJ*, 923, 69, doi: [10.3847/1538-4357/ac23df](https://doi.org/10.3847/1538-4357/ac23df)
- Ponti, G., George, E., Scaringi, S., et al. 2017, *MNRAS*, 468, 2447, doi: [10.1093/mnras/stx596](https://doi.org/10.1093/mnras/stx596)
- Porquet, D., Grosso, N., Predehl, P., et al. 2008, *A&A*, 488, 549, doi: [10.1051/0004-6361:200809986](https://doi.org/10.1051/0004-6361:200809986)
- Primiani, R. A., Young, K. H., Young, A., et al. 2016, *Journal of Astronomical Instrumentation*, 5, 1641006, doi: [10.1142/S2251171716410063](https://doi.org/10.1142/S2251171716410063)
- Psaltis, D., Johnson, M., Narayan, R., et al. 2018, *ArXiv e-prints*. <https://arxiv.org/abs/1805.01242>
- Quataert, E. 2002, *ApJ*, 575, 855, doi: [10.1086/341425](https://doi.org/10.1086/341425)
- Rauch, C., Ros, E., Krichbaum, T. P., et al. 2016, *A&A*, 587, A37, doi: [10.1051/0004-6361/201527286](https://doi.org/10.1051/0004-6361/201527286)
- Rea, N., Esposito, P., Pons, J. A., et al. 2013, *ApJL*, 775, L34, doi: [10.1088/2041-8205/775/2/L34](https://doi.org/10.1088/2041-8205/775/2/L34)
- Rea, N., Coti Zelati, F., Viganò, D., et al. 2020, *ApJ*, 894, 159, doi: [10.3847/1538-4357/ab8387](https://doi.org/10.3847/1538-4357/ab8387)
- Reid, M. J., & Brunthaler, A. 2004, *ApJ*, 616, 872, doi: [10.1086/424960](https://doi.org/10.1086/424960)
- Rickett, B. J. 1990, *ARA&A*, 28, 561, doi: [10.1146/annurev.aa.28.090190.003021](https://doi.org/10.1146/annurev.aa.28.090190.003021)
- Roelofs, F., Johnson, M. D., Shiokawa, H., Doeleman, S. S., & Falcke, H. 2017, *ApJ*, 847, 55, doi: [10.3847/1538-4357/aa8455](https://doi.org/10.3847/1538-4357/aa8455)
- Scargle, J. D. 1998, *The Astrophysical Journal*, 504, 405, doi: [10.1086/306064](https://doi.org/10.1086/306064)
- Scargle, J. D., Norris, J. P., Jackson, B., & Chiang, J. 2013, *ApJ*, 764, 167, doi: [10.1088/0004-637X/764/2/167](https://doi.org/10.1088/0004-637X/764/2/167)



- Schödel, R., Morris, M. R., Muzic, K., et al. 2011, *A&A*, 532, A83, doi: [10.1051/0004-6361/201116994](https://doi.org/10.1051/0004-6361/201116994)
- Schwab, F. R., & Cotton, W. D. 1983, *AJ*, 88, 688, doi: [10.1086/113360](https://doi.org/10.1086/113360)
- Serabyn, E., Carlstrom, J., Lay, O., et al. 1997, *ApJL*, 490, L77, doi: [10.1086/311010](https://doi.org/10.1086/311010)
- Shcherbakov, R. V., Penna, R. F., & McKinney, J. C. 2012, *ApJ*, 755, 133, doi: [10.1088/0004-637X/755/2/133](https://doi.org/10.1088/0004-637X/755/2/133)
- Shen, Z.-Q., Lo, K. Y., Liang, M.-C., Ho, P. T. P., & Zhao, J.-H. 2005, *Nature*, 438, 62, doi: [10.1038/nature04205](https://doi.org/10.1038/nature04205)
- Smirnov, O. M. 2011a, *A&A*, 527, A106, doi: [10.1051/0004-6361/201016082](https://doi.org/10.1051/0004-6361/201016082)
- . 2011b, *A&A*, 527, A107, doi: [10.1051/0004-6361/201116434](https://doi.org/10.1051/0004-6361/201116434)
- . 2011c, *A&A*, 527, A108, doi: [10.1051/0004-6361/201116435](https://doi.org/10.1051/0004-6361/201116435)
- . 2011d, *A&A*, 531, A159, doi: [10.1051/0004-6361/201116764](https://doi.org/10.1051/0004-6361/201116764)
- Steel, S., Wielgus, M., Blackburn, L., Issaoun, S., & Johnson, M. 2019, EHT Memo Series, 2019-CE-03
- Stone, J. M., Marrone, D. P., Dowell, C. D., et al. 2016, *ApJ*, 825, 32, doi: [10.3847/0004-637X/825/1/32](https://doi.org/10.3847/0004-637X/825/1/32)
- Su, M., & Finkbeiner, D. P. 2012, *ApJ*, 753, 61, doi: [10.1088/0004-637X/753/1/61](https://doi.org/10.1088/0004-637X/753/1/61)
- Telesco, C. M., Davidson, J. A., & Werner, M. W. 1996, *ApJ*, 456, 541, doi: [10.1086/176678](https://doi.org/10.1086/176678)
- Thompson, A. R., Moran, J. M., & Swenson, Jr., G. W. 2017, *Interferometry and Synthesis in Radio Astronomy*, 3rd Edition (Springer International Publishing), doi: [10.1007/978-3-319-44431-4](https://doi.org/10.1007/978-3-319-44431-4)
- van Bemmell, I., Small, D., Kettenis, M., et al. 2019, *PoS(EVN2018)079*, arXiv:1904.11747, doi: [10.22323/1.344.0079](https://doi.org/10.22323/1.344.0079)
- van den Eijnden, J., A, A., B, B., & C, C. 2021, in prep., 00, 0, doi: TBD
- van Langevelde, H. J., Frail, D. A., Cordes, J. M., & Diamond, P. J. 1992, *ApJ*, 396, 686, doi: [10.1086/171750](https://doi.org/10.1086/171750)
- Čadež, A., Calvani, M., & Kostić, U. 2008, *A&A*, 487, 527, doi: [10.1051/0004-6361:200809483](https://doi.org/10.1051/0004-6361:200809483)
- Verner, D. A., Ferland, G. J., Korista, K. T., & Yakovlev, D. G. 1996, *ApJ*, 465, 487, doi: [10.1086/177435](https://doi.org/10.1086/177435)
- Vertatschitsch, L., Primiani, R., Young, A., et al. 2015, *PASP*, 127, 1226, doi: [10.1086/684513](https://doi.org/10.1086/684513)
- von Fellenberg, S. D., Gillessen, S., Graciá-Carpio, J., et al. 2018, *ApJ*, 862, 129, doi: [10.3847/1538-4357/aacd4b](https://doi.org/10.3847/1538-4357/aacd4b)
- Wajima, K., Hagiwara, Y., An, T., et al. 2016, *Astronomical Society of the Pacific Conference Series*, Vol. 502, *The East-Asian VLBI Network*, ed. L. Qain & D. Li, 81
- Wang, Q. D., Nowak, M. A., Markoff, S. B., et al. 2013, *Science*, 341, 981, doi: [10.1126/science.1240755](https://doi.org/10.1126/science.1240755)
- Weisskopf, M. C., Brinkman, B., Canizares, C., et al. 2002, *PASP*, 114, 1, doi: [10.1086/338108](https://doi.org/10.1086/338108)
- Whitney, A. R., Cappallo, R., Aldrich, W., et al. 2004, *Radio Science*, 39, RS1007, doi: [10.1029/2002RS002820](https://doi.org/10.1029/2002RS002820)
- Whitney, A. R., Beaudoin, C. J., Cappallo, R. J., et al. 2013, *PASP*, 125, 196, doi: [10.1086/669718](https://doi.org/10.1086/669718)
- Wielgus, M., Blackburn, L., Issaoun, S., et al. 2019, EHT data set validation and characterization of errors, Tech. Rep. 2019-CE-02, EHT Memo Series
- Wielgus, M., Marchili, N., Martí-Vidal, I., et al. 2022, in prep., 00, 0, doi: TBD
- Williams, P. K. G., Clavel, M., Newton, E., & Ryzhkov, D. 2017, *pwkit: Astronomical utilities in Python*, <http://ascl.net/1704.001>
- Wilms, J., Allen, A., & McCray, R. 2000, *ApJ*, 542, 914, doi: [10.1086/317016](https://doi.org/10.1086/317016)
- Witzel, G., Eckart, A., Bremer, M., et al. 2012, *ApJS*, 203, 18, doi: [10.1088/0067-0049/203/2/18](https://doi.org/10.1088/0067-0049/203/2/18)
- Witzel, G., Martinez, G., Hora, J., et al. 2018a, *ApJ*, 863, 15, doi: [10.3847/1538-4357/aace62](https://doi.org/10.3847/1538-4357/aace62)
- . 2018b, *ApJ*, 863, 15, doi: [10.3847/1538-4357/aace62](https://doi.org/10.3847/1538-4357/aace62)
- Witzel, G., Martinez, G., Willner, S. P., et al. 2021, *ApJ*, 917, 73, doi: [10.3847/1538-4357/ac0891](https://doi.org/10.3847/1538-4357/ac0891)
- Wright, M. C. H., Genzel, R., Güsten, R., & Jaffe, D. T. 1987, in *American Institute of Physics Conference Series*, Vol. 155, *The Galactic Center*, ed. D. C. Backer, 133–137, doi: [10.1063/1.36411](https://doi.org/10.1063/1.36411)
- Young, A., Primiani, R., Weintroub, J., et al. 2016, in *Phased Array Systems and Technology (ARRAY, E1)*, doi: [10.1109/ARRAY.2016.7832576](https://doi.org/10.1109/ARRAY.2016.7832576)
- Yuan, F., Quataert, E., & Narayan, R. 2003, *ApJ*, 598, 301, doi: [10.1086/378716](https://doi.org/10.1086/378716)
- Yusef-Zadeh, F., Bushouse, H., Schödel, R., et al. 2015, *ApJ*, 809, 10, doi: [10.1088/0004-637X/809/1/10](https://doi.org/10.1088/0004-637X/809/1/10)
- Yusef-Zadeh, F., Morris, M., & Ekers, R. D. 1990, *Nature*, 348, 45, doi: [10.1038/348045a0](https://doi.org/10.1038/348045a0)
- Yusef-Zadeh, F., Wardle, M., Miller-Jones, J. C. A., et al. 2011, *ApJ*, 729, 44, doi: [10.1088/0004-637X/729/1/44](https://doi.org/10.1088/0004-637X/729/1/44)
- Yusef-Zadeh, F., Arendt, R., Bushouse, H., et al. 2012, *ApJL*, 758, L11, doi: [10.1088/2041-8205/758/1/L11](https://doi.org/10.1088/2041-8205/758/1/L11)
- Zhang, S., Baganoff, F. K., Ponti, G., et al. 2017a, *ApJ*, 843, 96, doi: [10.3847/1538-4357/aa74e8](https://doi.org/10.3847/1538-4357/aa74e8)
- . 2017b, *ApJ*, 843, 96, doi: [10.3847/1538-4357/aa74e8](https://doi.org/10.3847/1538-4357/aa74e8)
- Zhao, J.-H., Young, K. H., Herrnstein, R. M., et al. 2003, *ApJL*, 586, L29, doi: [10.1086/374581](https://doi.org/10.1086/374581)
- Zheng, W. 2015, in *IAU General Assembly*, Vol. 29, 2255896
- Zhu, Z., Li, Z., Morris, M. R., Zhang, S., & Liu, S. 2019, *ApJ*, 875, 44, doi: [10.3847/1538-4357/ab0e05](https://doi.org/10.3847/1538-4357/ab0e05)

- Zubovas, K., Nayakshin, S., & Markoff, S. 2012, Monthly Notices of the Royal Astronomical Society, 421, 1315, doi: [10.1111/j.1365-2966.2011.20389.x](https://doi.org/10.1111/j.1365-2966.2011.20389.x)
- Zylka, R., & Mezger, P. G. 1988, A&A, 190, L25
- Zylka, R., Mezger, P. G., & Lesch, H. 1992, A&A, 261, 119
- Zylka, R., Mezger, P. G., Ward-Thompson, D., Duschl, W. J., & Lesch, H. 1995, A&A, 297, 83.  
<https://arxiv.org/abs/astro-ph/9410086>